

# Water Resources Research

## RESEARCH ARTICLE

10.1029/2019WR024840

### Key Points:

- A full Bayesian method is proposed for model selection among geologically realistic conceptual models
- Thermodynamic integration and stepping-stone sampling provide consistent ranking of conceptual models
- The method is applied to solute concentration data collected during a tracer test at the MADE site

### Supporting Information:

- Supporting Information S1

### Correspondence to:

C. Brunetti,  
Carlotta.Brunetti@unil.ch

### Citation:

Brunetti, C., Bianchi, M., Pirot, G., & Linde, N. (2019). Hydrogeological model selection among complex spatial priors. *Water Resources Research*, 55, 6729–6753. <https://doi.org/10.1029/2019WR024840>

Received 24 JAN 2019

Accepted 2 JUL 2019

Accepted article online 5 JUL 2019

Published online 13 AUG 2019

## Hydrogeological Model Selection Among Complex Spatial Priors

C. Brunetti<sup>1</sup> , M. Bianchi<sup>2</sup> , G. Pirot<sup>1</sup> , and N. Linde<sup>1</sup> 

<sup>1</sup>Applied and Environmental Geophysics Group, Institute of Earth Sciences, University of Lausanne, Lausanne, Switzerland, <sup>2</sup>British Geological Survey, Environmental Science Centre, Nottingham, UK

**Abstract** Hydrogeological field studies rely often on a single conceptual representation of the subsurface. This is problematic since the impact of a poorly chosen conceptual model on predictions might be significantly larger than the one caused by parameter uncertainty. Furthermore, conceptual models often need to incorporate geological concepts and patterns in order to provide meaningful uncertainty quantification and predictions. Consequently, several geologically realistic conceptual models should ideally be considered and evaluated in terms of their relative merits. Here, we propose a full Bayesian methodology based on Markov chain Monte Carlo to enable model selection among 2-D conceptual models that are sampled using training images and concepts from multiple-point statistics. More precisely, power posteriors for the different conceptual subsurface models are sampled using sequential geostatistical resampling and Graph Cuts. To demonstrate the methodology, we compare and rank five alternative conceptual geological models that have been proposed in the literature to describe aquifer heterogeneity at the MACRODispersion Experiment site in Mississippi, USA. We consider a small-scale tracer test for which the spatial distribution of hydraulic conductivity impacts multilevel solute concentration data observed along a 2-D transect. The thermodynamic integration and the stepping-stone sampling methods were used to compute the evidence and associated Bayes factors using the computed power posteriors. We find that both methods are compatible with multiple-point statistics-based inversions and provide a consistent ranking of the competing conceptual models considered.

## 1. Introduction

The geological structure of the subsurface is a key controlling factor on groundwater flow and solute transport in aquifers (Maliva, 2016; Renard & Allard, 2013; Zheng & Gorelick, 2003), and, therefore, it needs to be properly represented and accounted for in modeling studies. The needs for quantitative and reliable subsurface modeling and management (Refsgaard & Henriksen, 2004; Scheidt et al., 2018) are driving hydrogeologists to consider conceptual models with increasing geological realism and complexity (e.g., see reviews by Hu & Chugunova, 2008; Linde et al., 2015a). Traditionally, (hydro)geological subsurface heterogeneity has often been described in terms of mean values and covariances of the relevant physical properties (e.g., through the widely used multi-Gaussian models). However, such conceptualizations may be too simplistic in certain subsurface systems and, therefore, insufficient to accurately reproduce and predict flow and transport processes (Gómez-Hernández & Wen, 1998; Journel & Zhang, 2006; Kerrou et al., 2008; Zinn & Harvey, 2003). Multiple-point statistics (MPS) (Guardiano & Srivastava, 1993; Hu & Chugunova, 2008; Mariethoz & Caers, 2014; Strebelle, 2002) offers a means to effectively reproduce complex geological structures such as curvilinear features. By using a training image, MPS enables geostatistical simulations that honor point data and the higher-order spatial statistics that are captured in the training image. The training image is a conceptual representation summarizing prior geological understanding about the system under study. It can be constructed from sketches drawn by hand or digitalized outcrops, or generated by, for example, process-imitating, structure-imitating, or descriptive simulation methods (De Marsily et al., 2005; Koltermann & Gorelick, 1996).

In many real world applications, generally because of the sparsity of direct observations, several alternative conceptualizations of subsurface heterogeneity (e.g., describing the spatial distribution of hydraulic conductivity) might be plausible and proposed by one or several experts. Unfortunately, uncertainty pertaining to the choice of the conceptual model is often ignored in modeling studies, even if it might be a dominant source of uncertainty (Bond et al., 2007; Lark et al., 2014; Randle et al., 2018; Refsgaard et al., 2012; Rojas et al.,

2008; Scheidt et al., 2018). Indeed, geostatistical model realizations generated from one training image might lead to a vastly different range of predictions than those generated from another training image, as shown, for example, by Pirot et al. (2015). Conceptual uncertainty should, therefore, be integrated in modeling and inversion studies. Ideally, this should be achieved by using formal methods to test and rank alternative conceptual geological models based on available hydrogeological and geophysical data (Dettmer et al., 2010; Linde, 2014; Linde et al., 2015a; Schöniger et al., 2014). Bayesian model selection (Jeffreys, 1935, 1939; Kass & Raftery, 1995) offers a quantitative approach to perform such comparisons by computing the so-called evidence (i.e., the denominator in Bayes' theorem) which allows to identify the conceptual model, in a chosen set, that is the most supported by the data. However, a complication arises when performing Bayesian model selection with complex spatial priors that are represented by training images. Most MPS-based inversions are nonparametric, which implies that they rely on samples being drawn proportionally to the prior distribution, while it is generally not possible within a MPS framework to evaluate the prior probability of a given model proposal. Hence, MPS-based inversions cannot build on many state-of-the-art concepts to enhance the performance of the Markov chain Monte Carlo (MCMC) (e.g., Laloy & Vrugt, 2012) and associated approaches for calculating the evidence (Brunetti et al., 2017; Volpi et al., 2017). Similarly, it is not possible within a MPS framework to calculate approximate evidence estimates using the Laplace-Metropolis method (Lewis & Raftery, 1997).

It is only recently that MPS-based inversions have been proposed (see review by Linde et al., 2015a). MCMC inversions with MPS (e.g., Hansen et al., 2012; Mariethoz et al., 2010a) generally rely on model proposals obtained by sequential geostatistical resampling of the prior (Gibbs sampling) that are used within the extended Metropolis algorithm to accept model proposals based on the likelihood ratio (Mosegaard & Tarantola, 1995). Sequential geostatistical resampling generates model proposals of the spatially distributed parameters of interest by conditional resimulations of a random fraction of the current field proportional to the prior as defined by the training image. There exist several MPS methods to sample complex spatial priors with sequential Gibbs sampling. Examples include the versatile direct sampling method (Mariethoz et al., 2010) or the recent Graph Cuts approach (Li et al., 2016; Zahner et al., 2016) that enables speed-ups by 1 to 2 orders of magnitude. Since high-dimensional MCMC inversions necessitate many evaluations of model proposals by forward modeling, it is essential that the geostatistical model proposal process is fast compared to the forward simulation time while ensuring model realizations of high quality that honor geological patterns in the training image. Various advances have been made to enhance MPS-based inversions both in a nonparametric MCMC framework (e.g., parallel tempering by Laloy et al., 2016) and in a parametric framework using, for example, spatial generative adversarial neural networks (Laloy et al., 2018). Also, ensemble-based exploration schemes have been explored (Jäggli et al., 2017).

State-of-the-art evidence estimators that are compatible with nonparametric spatial priors include thermodynamic integration (Friel & Pettitt, 2008a; Gelman & Meng, 1998) and stepping-stone (Xie et al., 2011) and nested sampling (Skilling, 2004, 2006). The thermodynamic integration method takes the name from its original application, which was to compute the difference in a thermodynamic property (usually free energy) of a system at two given states. Thermodynamic integration and the stepping-stone method sample from a sequence of so-called power posterior distributions that connect the prior to the posterior distribution. The nested sampling method is based on a constrained local sampling procedure in which the prior distribution is sampled under the constraint of a lower bound on the log likelihood function that increases with time. Thermodynamic integration and nested sampling transform the evidence, that is, a multidimensional integral over the parameter space, into a one-dimensional integral over unit range in the log likelihood space. The stepping-stone sampling estimator approximates the evidence by importance sampling using the power posteriors as importance distributions. To the best of our knowledge, thermodynamic integration and stepping-stone sampling have never been used to estimate the evidence of subsurface models built with MPS in the context of Bayesian model selection, while this is the case for nested sampling (Elsheikh et al., 2015). Recent studies in hydrology suggest that nested sampling is less accurate and stable than thermodynamic integration (Liu et al., 2016; Zeng et al., 2018) and that it is strongly dependent on the efficiency of the constrained local sampling procedure. Unfortunately, MPS-based inversions cannot benefit from recent improvements in constrained local sampling approaches as they require parametric (analytical) forms of the prior (Cao et al., 2018; Liu et al., 2016; Schöniger et al., 2014; Zeng et al., 2018). Even if thermodynamic integration and stepping-stone sampling are computationally expensive, they are easily parallelized such that the computational time is equivalent to the time needed to run a single MCMC chain. Moreover, these

two methods are easy to implement and flexible in the sense that any suitable MCMC method can, provided minimal changes, be used to explore the power posterior distributions. The classical brute force Monte Carlo method (Hammersley & Handscomb, 1964) can also be used to estimate the evidence when considering nonparametric spatial priors. However, Brunetti et al. (2017) show that Monte Carlo often requires a prohibitive computational time to obtain reliable evidence estimates even for very simple subsurface conceptualizations (e.g., layered models) when considering as few as seven unknowns. This limits its application to realistic high-dimensional MPS-based conceptual models.

One way to circumvent the challenges of nonparametric priors in Bayesian model selection is to reduce the model parameter space, for example, by cluster-based polynomial chaos expansion (Bazargan & Christie, 2017) or by truncated discrete cosine transform combined with summary metrics from training images (Lochbühler et al., 2015). Bayesian inference and model selection is then applied on the reduced dimension space whose prior distribution is parametric (e.g., multivariate Gaussian distribution). The main drawback of such approaches is that truncation may smoothen sharp interfaces found in the training images.

In this study, we propose the first full Bayesian method that enables Bayesian model selection among geologically realistic conceptual subsurface models. To do so, we combine sequential geostatistical resampling based on Graph Cuts, the extended Metropolis acceptance criterion and evidence estimation by power posteriors using either thermodynamic integration or stepping-stone sampling. The advantages and the drawbacks of this new methodology are assessed using a challenging application. In this study, we compare and rank five alternative conceptual geological models that have been proposed in the literature to characterize the spatial heterogeneity of the aquifer at the Macrodispersion Experiment (MADE) site in Mississippi, USA (Zheng et al., 2011). Among this set of five conceptual models of hydraulic conductivity spatial distribution, we aim to identify the one that is in the best agreement with multilevel concentration data acquired during a small-scale dipole tracer test (MADE-5) (Bianchi, Zheng, Tick, et al., 2011). The case study at the MADE site is used to demonstrate the ability of our Bayesian model selection method to deal with widely different conceptual hydrogeological models. We stress that the 2-D modeling framework used herein limits our ability to generalize the findings to actual 3-D field conditions. Extensions to 3-D is methodologically straightforward but computationally very challenging.

## 2. Theory

### 2.1. Bayesian Inference and Model Selection

Bayesian inference approaches express the posterior probability density function (pdf),  $p(\boldsymbol{\theta}|\tilde{\mathbf{Y}})$ , of a set of unknown model parameters,  $\boldsymbol{\theta} = \{\theta_1, \dots, \theta_d\}$ , given  $n$  measurements,  $\tilde{\mathbf{Y}} = \{\tilde{y}_1, \dots, \tilde{y}_n\}$ , via Bayes' theorem

$$p(\boldsymbol{\theta}|\tilde{\mathbf{Y}}) = \frac{p(\boldsymbol{\theta})p(\tilde{\mathbf{Y}}|\boldsymbol{\theta})}{p(\tilde{\mathbf{Y}})}. \quad (1)$$

The prior pdf,  $p(\boldsymbol{\theta})$ , quantifies all the information that is available about the model parameters before considering the observed data. Typically,  $p(\boldsymbol{\theta})$  is represented by multivariate analytical functions (e.g., Gaussian, uniform, and exponential) describing marginal distributions of each parameter and their spatial correlation. With the advent of MPS methods, higher-order spatial statistics of  $\boldsymbol{\theta}$  can be incorporated in inversions by means of training images. In this case, the description of prior knowledge is typically nonparametric and sequential geostatistical resampling techniques are used to sample  $p(\boldsymbol{\theta})$ . The likelihood function,  $p(\tilde{\mathbf{Y}}|\boldsymbol{\theta})$ , summarizes in a single scalar value the probability that the observed data have been generated by a proposed set of model parameters. We consider a Gaussian likelihood characterized by uncorrelated and normally distributed measurement errors with constant standard deviation,  $\sigma_{\tilde{\mathbf{Y}}}$ ,

$$p(\tilde{\mathbf{Y}}|\boldsymbol{\theta}) = \left(\sqrt{2\pi\sigma_{\tilde{\mathbf{Y}}}^2}\right)^{-n} \exp\left[-\frac{1}{2}\sum_{h=1}^n \left[\frac{\tilde{y}_h - \mathcal{F}_h(\boldsymbol{\theta})}{\sigma_{\tilde{\mathbf{Y}}}}\right]^2\right]. \quad (2)$$

As the residuals between the observed data,  $\tilde{y}_h$ , and the simulated forward responses,  $\mathcal{F}_h(\boldsymbol{\theta})$ , tend toward 0, the likelihood increases and, in particular,  $p(\tilde{\mathbf{Y}}|\boldsymbol{\theta}) \rightarrow \left(\sqrt{2\pi\sigma_{\tilde{\mathbf{Y}}}^2}\right)^{-n}$ . The denominator in Bayes' theorem is the evidence (or marginal likelihood),  $p(\tilde{\mathbf{Y}})$ , and it is the cornerstone quantity in most Bayesian model selection problems. It should be noted, however, that the explicit computation of the evidence can be avoided by using reversible jump (transdimensional) MCMC methods (Green, 1995). The conceptual model with the highest

evidence (Jeffreys, 1935, 1939) is the one that is the most supported by the data. A noteworthy feature of the evidence is that it implicitly accounts for the trade-off between goodness of fit and model complexity (Gull, 1988; Jeffreys, 1939; Jefferys & Berger, 1992; MacKay, 1992). More precisely, the evidence quantifies how likely it is that a given conceptual model,  $\eta \in \mathbb{N}$ , with model parameters,  $\theta$ , and prior distribution,  $p(\theta|\eta)$ , has generated the data  $\tilde{\mathbf{Y}}$ ,

$$p(\tilde{\mathbf{Y}}|\eta) = \int p(\tilde{\mathbf{Y}}|\theta, \eta)p(\theta|\eta)d\theta. \quad (3)$$

The evidence is used to calculate Bayes factors (Kass & Raftery, 1995), that is, evidence ratios of one conceptual model with respect to another. For instance, the Bayes factor of  $\eta_1$  with respect to  $\eta_2$ , or  $B_{(\eta_1, \eta_2)}$ , is defined as

$$B_{(\eta_1, \eta_2)} = \frac{p(\tilde{\mathbf{Y}}|\eta_1)}{p(\tilde{\mathbf{Y}}|\eta_2)}. \quad (4)$$

Conceptual models with large Bayes factors are preferred statistically, and the conceptual model with the largest evidence is the one that best honors the data on average over its prior. However, the evidence computation is analytically intractable for most problems of interest and the multidimensional integral in equation (3) must be approximated by numerical means. In this work, the different conceptual models represent alternative spatial representations of hydraulic conductivity in the subsurface.

## 2.2. Evidence Estimation by Power Posteriors

Thermodynamic integration, also called path sampling (Gelman & Meng, 1998), and stepping-stone sampling (Xie et al., 2011) are two methods to estimate the evidence (equation (3)) numerically. The key idea behind both methods is to sample from a sequence of so-called power posterior distributions,  $p_\beta(\theta|\tilde{\mathbf{Y}})$ , in order to create a path in the probability density space that connects the prior to the posterior distribution (Friel & Pettitt, 2008a). The power posterior distribution is proportional to the prior pdf multiplied by the likelihood function raised to the power of  $\beta \in [0, 1]$ :

$$p_\beta(\theta|\tilde{\mathbf{Y}}) \propto p(\theta)p(\tilde{\mathbf{Y}}|\theta)^\beta. \quad (5)$$

Decreasing  $\beta$  has the effect of flattening the likelihood function. For  $\beta = 1$ , the posterior distribution is sampled,  $p_1(\theta|\tilde{\mathbf{Y}}) \propto p(\theta)p(\tilde{\mathbf{Y}}|\theta)$ ; for  $\beta = 0$ , the prior distribution is sampled,  $p_0(\theta|\tilde{\mathbf{Y}}) \propto p(\theta)$ . In thermodynamic integration and stepping-stone sampling, the priors are assumed to be proper and a sequence of  $\beta$  values needs to be defined (see section 2.2.3). For each  $\beta$  value, one (or more) MCMC runs are used to draw  $N$  samples from the corresponding power posterior distribution and the corresponding likelihood values are recorded. The Markov chains for the different  $\beta$  values can be run independently in parallel or sequentially from  $\beta = 0$  to  $\beta = 1$  (serial MCMC) as described in Friel and Pettitt (2008a). Thermodynamic integration and stepping-stone sampling have several attractive characteristics: (1) the total computing time is equivalent to a normal MCMC inversion provided that all MCMC runs are carried out in parallel, (2) they can be applied for any MCMC inversion method with only minimal intervention (it is only necessary to add the exponent  $\beta$  to the likelihood function), and (3) the only information needed is the series of likelihoods obtained from MCMC simulations with different  $\beta$  values. Once the power posterior distributions have been sampled, the thermodynamic integration and stepping-stone sampling methods use the recorded likelihood values in two different ways to estimate the evidence (sections 2.2.1–2.2.2).

### 2.2.1. Thermodynamic Integration

Thermodynamic integration reduces the multidimensional integral of equation (3) into a one-dimensional integral of the expectation of the log likelihood,  $\log p(\tilde{\mathbf{Y}}|\theta, \eta)$ , as

$$\log p(\tilde{\mathbf{Y}}|\eta) = \int_0^1 E_{\theta|\tilde{\mathbf{Y}}, \beta} \left[ \log p(\tilde{\mathbf{Y}}|\theta, \eta) \right] d\beta. \quad (6)$$

For the derivation of equation (6), we refer to Friel and Pettitt (2008a) and Lartillot and Philippe (2006). The integral in equation (6) is estimated by a quadrature approximation over a discrete set of  $\beta$  values,  $0 = \beta_1 < \dots < \beta_j < \dots < \beta_J = 1$ . To simplify the notation, we define the expectations of the log likelihood

functions as  $\ell_j \equiv E_{\theta|\tilde{\mathbf{Y}},\beta_j} [\log p(\tilde{\mathbf{Y}}|\theta, \eta)]$  and their corresponding variances as  $\sigma_j^2 \equiv V_{\theta|\tilde{\mathbf{Y}},\beta_j} [\log p(\tilde{\mathbf{Y}}|\theta, \eta)]$ . In this work, we use the corrected composite trapezoidal rule:

$$\log p(\tilde{\mathbf{Y}}|\eta) \approx \sum_{j=2}^J \frac{(\beta_j - \beta_{j-1})}{2} (\ell_j + \ell_{j-1}) - \sum_{j=2}^J \frac{(\beta_j - \beta_{j-1})^2}{12} (\sigma_j^2 - \sigma_{j-1}^2), \quad (7)$$

which provides more accurate estimates compared with the classical composite trapezoidal rule (first term in equation (7)) as it also considers the second-order correction term (second term in equation (7)). This corrected composite trapezoidal rule was originally employed by Friel et al. (2014) and later used by other authors including Oates et al. (2016) and Grzegorzczuk et al. (2017).

The accuracy of the resulting evidence estimates depends on how the  $\beta$  values are discretized, the number of  $\beta$  values used,  $J$  (details provided in section 2.2.3), the number,  $N$ , and the degree of correlation of the power posterior samples obtained by MCMC. The uncertainties associated with the evidence estimation by thermodynamic integration are often summarized by two error types: the sampling error,  $e_s$ , and the discretization error,  $e_d$  (Calderhead & Girolami, 2009; Lartillot & Philippe, 2006). The sampling error is related to the standard errors of the MCMC posterior expectations of the log likelihoods obtained for each  $\beta_j$ . To avoid underestimation of these errors, the autocorrelation in the MCMC samples should be accounted for in order to calculate the effective sample size,  $N_{\text{eff}}$ , (i.e., number of independent samples within each MCMC chain) as suggested by Kass et al. (1998). The effective sample size is defined as

$$N_{\text{eff},j} = \frac{N_j}{1 + 2 \sum_{z=1}^{\infty} \rho_j(z)}, \quad (8)$$

where  $\rho_j(z)$  is the autocorrelation at lag  $z$ . Applying the rules for uncertainty propagation to the first leading term in equation (7) and assuming the errors of  $\ell_j$  to be independent of those associated to  $\ell_{j-1}$ , the sampling error is

$$\sigma_s^2 = \sum_{j=2}^J \frac{(\beta_j - \beta_{j-1})^2}{4} \left( \frac{\sigma_j^2}{N_{\text{eff},j}} + \frac{\sigma_{j-1}^2}{N_{\text{eff},j-1}} \right). \quad (9)$$

Discretization errors arise as the continuous integral of equation (6) is estimated using a finite number of evaluation points (equation (7)). Following Lartillot and Philippe (2006), Baele et al. (2013), and Friel et al. (2014), we define  $e_d$  as the worst case discretization error that arises from the approximation of equation (6) with a rectangular rule. Hence,  $e_d$  is half the difference of the areas between the upper and lower step functions and it can be interpreted as the variance of the trapezoidal rule:

$$\sigma_d^2 = \sum_{j=2}^J \frac{(\beta_j - \beta_{j-1})^2}{4} (\ell_j - \ell_{j-1})^2. \quad (10)$$

As a consequence, the variance on the evidence estimates can be summarized as  $\hat{\text{Var}} \log p(\tilde{\mathbf{Y}}|\eta) = \sigma_d^2 + \sigma_s^2$ .

### 2.2.2. Stepping-Stone Sampling

Stepping-stone sampling (Xie et al., 2011) computes the evidence by combining power posteriors with importance sampling. The key underlying idea is to write the evidence as the ratio,  $r$ , of the normalizing factors in Bayes' theorem for  $\beta = 1$  (posterior sampling) and  $\beta = 0$  (prior sampling):

$$r = \frac{p(\tilde{\mathbf{Y}}|\eta, \beta = 1)}{p(\tilde{\mathbf{Y}}|\eta, \beta = 0)}. \quad (11)$$

Since the prior integrates to 1, the evidence is equivalent to  $r$  as  $p(\tilde{\mathbf{Y}}|\eta, \beta = 0)$  equals 1. The ratio can be expressed as a product of  $J$  ratios,  $r_j$ :

$$r = \prod_{j=2}^J r_{j-1} = \prod_{j=2}^J \frac{p(\tilde{\mathbf{Y}}|\eta, \beta_j)}{p(\tilde{\mathbf{Y}}|\eta, \beta_{j-1})}. \quad (12)$$

Then, importance sampling is applied to the numerator and denominator of equation (12) using the power posterior  $p_{\beta_{j-1}}(\boldsymbol{\theta}|\tilde{\mathbf{Y}})$  as the importance distribution:

$$r_{j-1} = \frac{1}{N} \sum_{i=1}^N p(\tilde{\mathbf{Y}}|\boldsymbol{\theta}_{j-1,i})^{\beta_j - \beta_{j-1}} \quad (13)$$

and, finally, the log-evidence is computed as

$$\log p(\tilde{\mathbf{Y}}|\eta) = \sum_{j=2}^J \log r_{j-1} = \sum_{j=2}^J \log \left\{ \frac{1}{N} \sum_{i=1}^N \exp \left[ (\beta_j - \beta_{j-1}) \cdot \log p(\tilde{\mathbf{Y}}|\boldsymbol{\theta}_{j-1,i}) \right] \right\}. \quad (14)$$

In contrast to thermodynamic integration, the evidence estimated by stepping-stone sampling does not suffer from discretization errors. The sampling error can be evaluated as

$$\widehat{\text{Var}} \log p(\tilde{\mathbf{Y}}|\eta) = \sum_{j=2}^J \frac{1}{N_{\text{eff},j-1} \cdot N} \sum_{i=1}^N \left( \frac{p(\tilde{\mathbf{Y}}|\boldsymbol{\theta}_{j-1,i})^{\beta_j - \beta_{j-1}}}{r_{j-1}} - 1 \right)^2. \quad (15)$$

The derivation of equations (14) and (15) appears in Fan et al. (2011) and Xie et al. (2011), and interested readers are referred to this publication for further details. The only difference in our equation (15) is that we consider the effective sample size as defined in equation (8). Note that equation (13) is only valid for the specific choice of  $p_{\beta_{j-1}}(\boldsymbol{\theta}|\tilde{\mathbf{Y}})$  as the importance distribution.

### 2.2.3. Discretization Scheme for $\beta$ Values

For small increases of  $\beta$  close to 0,  $l_j$  increases dramatically and the corresponding power posteriors quickly turn from being similar to the prior to being similar to the posterior distribution (e.g., Friel et al., 2014; Liu et al., 2016; Oates et al., 2016). As a consequence, the accuracy of the evidence estimates increases when placing most of the  $\beta$  values close to 0 (e.g., Friel & Pettitt, 2008b; Grzegorzczak et al., 2017; Liu et al., 2016). This is especially true for the thermodynamic integration method that estimates the evidence as the area below the curve of the expectation of the log likelihood,  $l_j$ , as a function of  $\beta_j$  (equation (6)). Starting from an initial set of sampling points, Liu et al. (2016) use an empirical method that places additional  $\beta$  values based on a qualitative search for locations where  $l_j$  changes strongly in order to target additional  $\beta$  values to use. However, this method is subjective and it increases the computing time when using parallel computations as the  $\beta$  values are not defined at the outset. Friel and Pettitt (2008a) are the first to employ a discretization scheme of  $\beta$  values that follows a power law spacing as

$$\beta_j = \left( \frac{j-1}{J-1} \right)^c \quad \text{with } j = 1, 2, \dots, J. \quad (16)$$

Calderhead and Girolami (2009) demonstrate that this scheme significantly improves the accuracy of the evidence estimates with respect to the uniform spacing used by Lartillot and Philippe (2006).

## 3. Method

### 3.1. General Framework

It is common to sample the unnormalized posterior pdf of equation (1) with MCMC simulations. This is here achieved by combining the extended Metropolis acceptance criterion (Mosegaard & Tarantola, 1995) with a sequential geostatistical resampling technique (e.g., Graph Cuts) that provides conditional model proposals at each iteration featuring similar geological patterns as those found in the corresponding training image. For each proposed model,  $\boldsymbol{\theta}_{\text{prop}}$ , we calculate the forward response and compare it with the observed data and, according to the extended Metropolis algorithm, accept  $\boldsymbol{\theta}_{\text{prop}}$  with probability

$$\alpha = \min \left\{ 1, \frac{p(\tilde{\mathbf{Y}}|\boldsymbol{\theta}_{\text{prop}})}{p(\tilde{\mathbf{Y}}|\boldsymbol{\theta}_{\text{cur}})} \right\}. \quad (17)$$

To sample the power posteriors, we simply modify the extended Metropolis acceptance criteria by raising the likelihoods in equation (17) with the corresponding  $\beta_k$  values. We report below the overall algorithm

(Algorithm 1), in which we combine model proposals based on MPS with the extended Metropolis acceptance criteria followed by evidence estimation using power posteriors.

---

**Algorithm 1:** MCMC inversion workflow based on MPS and the extended Metropolis

algorithm to enable evidence estimation using power posteriors.

---

**Input:**  $T$ , maximum number of MCMC iterations;  $J$ , number of power coefficients  $\beta$  distributed according to Eq. 16; a training image

**Output:**  $\Lambda_j$ , matrices containing power posteriors and log-likelihoods;  $\log p(\tilde{\mathbf{Y}}|\eta)$ , evidence

Set  $t = 1$ ;

Draw  $\theta_1$  from the training image;

Solve the forward problem;

Compute likelihood (e.g., Eq. 2);

**for**  $j = 1, \dots, J$  **do**

**for**  $t = 2, \dots, T$  **do**

Set  $\theta_{\text{cur}} = \theta_{t-1}$ ;

Draw  $\theta_{\text{prop}}$  based on MPS (e.g., using Graph Cuts proposals);

Solve the forward problem;

Compute likelihood (e.g., Eq. 2);

Accept  $\theta_{\text{prop}}$  with probability,  $\alpha = \min \left\{ 1, \frac{p(\tilde{\mathbf{Y}}|\theta_{\text{prop}})^{\beta_j}}{p(\tilde{\mathbf{Y}}|\theta_{\text{cur}})^{\beta_j}} \right\}$ ;

**if**  $\theta_{\text{prop}}$  *accepted* **then**

Set  $\theta_t = \theta_{\text{prop}}$ ;

**else**

Set  $\theta_t = \theta_{\text{cur}}$ ;

**end**

Store  $\theta_t$  and the corresponding log-likelihood in matrix  $\Lambda_j$ ;

Set  $t=t+1$ ;

**end**

**end**

Compute  $\log p(\tilde{\mathbf{Y}}|\eta)$  (Eqs. 7 and 14) and corresponding variances (Eqs. 9-10 and 15) using the information stored in  $\Lambda_j$  after the removal of the burn-in period.

---

### 3.2. Graph Cuts Model Proposals

In this work, to sample spatially correlated parameters, we rely on model proposals based on the Graph Cuts algorithm introduced by Zahner et al. (2016) with some of the improvements proposed by Pirot et al. (2017, 2017b). The main steps in the Graph Cuts algorithm are depicted in Figure 1. Basically, a section of the same size as the model domain,  $\theta_{\text{new}}$  (Figure 1b) is randomly drawn from the training image and

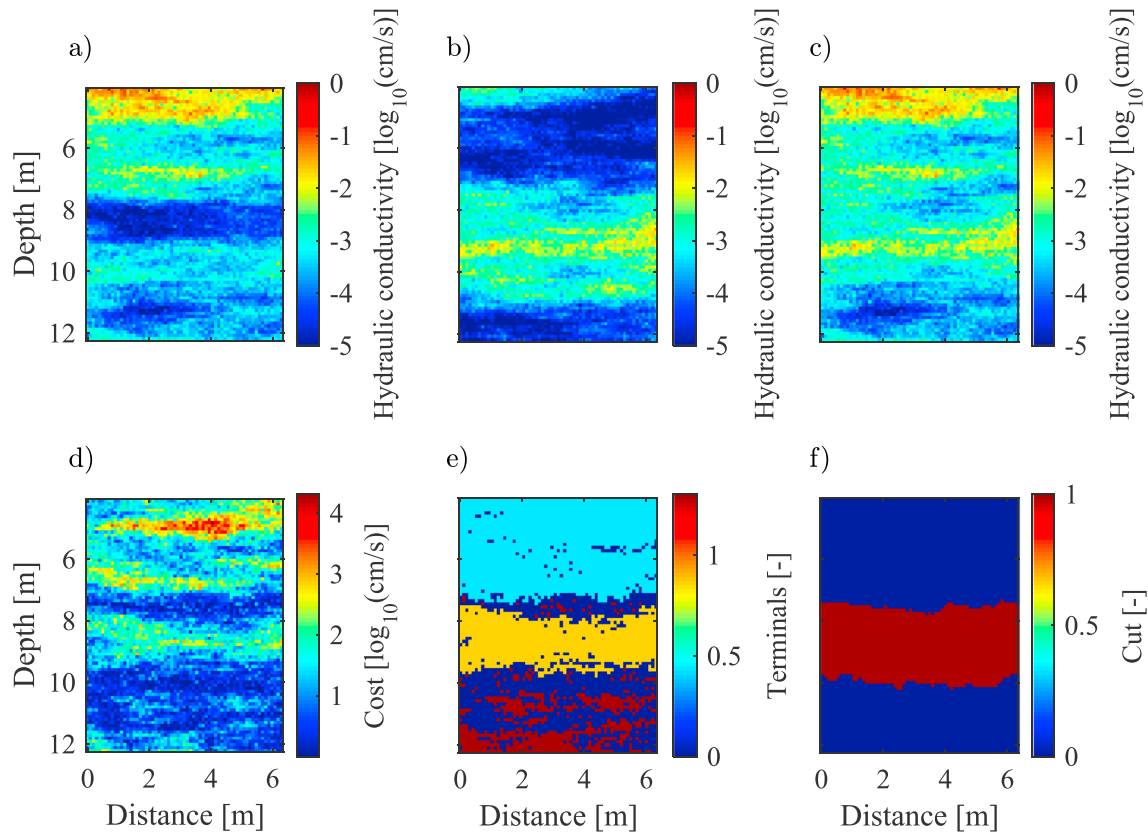


**Figure 1.** Illustration of how model proposals are obtained using the Graph Cuts algorithm. (a) Current model realization,  $\theta_{\text{cur}}$ , (b) section drawn randomly from the training image,  $\theta_{\text{new}}$ , and (c) the resulting model proposal,  $\theta_{\text{prop}}$ . This model proposal is obtained as follows: (d) the cost image,  $\delta$ , is defined as the absolute difference raised to the cost power,  $\delta_{cp}$ , that is  $\delta = |\theta_{\text{cur}} - \theta_{\text{new}}|^{\delta_{cp}}$ , (e) two disconnected regions of high differences (light blue and orange areas) of similar size are randomly selected, and (f) the cut of minimum cost that separates the two regions is calculated, and the resulting dark red region is cut from (b)  $\theta_{\text{new}}$  and pasted into (a)  $\theta_{\text{cur}}$  to create (c)  $\theta_{\text{prop}}$ .

the absolute difference between  $\theta_{\text{new}}$  and the current model realization,  $\theta_{\text{cur}}$  (Figure 1a), is computed and raised to the power of the cost power,  $\delta_{cp}$ , (Pirot et al., 2017b) to obtain the cost image,  $\delta = |\theta_{\text{cur}} - \theta_{\text{new}}|^{\delta_{cp}}$  (Figure 1d). Two distinct regions of high cost and similar size and containing at least  $p$  pixels are randomly selected (Figure 1e). To choose these terminals, Pirot, Linde, et al. (2017) introduce the cutting threshold,  $\delta_{th} \in [0, 100]$ , defined as a percentile of  $\max(\delta)$ , which limits the possible terminals to those regions where  $\delta > \delta_{th} \cdot \max(\delta)$ . A patch is defined as the region enclosed by a minimum cost line separating the two terminals using the min-cut/max-flow algorithm by Boykov and Kolmogorov (2004; Figure 1f), and the new model proposal,  $\theta_{\text{prop}}$  (Figure 1c), is built by cutting the patch from  $\theta_{\text{new}}$  and replacing the corresponding area in  $\theta_{\text{cur}}$ .

We manually tune three algorithmic parameters to obtain model proposals that preserve the patterns found in the training image: the minimum number,  $p$ , of pixels in each of the two terminals, the cutting threshold,  $\delta_{th}$ , and the cost power,  $\delta_{cp}$ . We have set the cost power to 1 or 2 depending on the type of conceptual model considered. The main reason for using graph-cut proposals in this work is its computational speed relative to other MPS algorithms (see comparisons by Zahner et al., 2016). However, slower pixel-based geostatistical resimulation strategies that implement sequential Gibbs sampling, such as those presented by Mariethoz, Renard, and Straubhaar (2010) or Hansen et al. (2012), could also be used.

### 3.3. Field Site and Available Data

The MADE site is characterized by an unconsolidated shallow alluvial aquifer composed by a mixture of gravel, sand, and finer sediments. The high heterogeneity at the MADE site got the attention of the hydrogeological community in the mid-1980s, and numerous studies have been carried out since then (see Zheng et al., 2011 for a review). Previous interpretations of two large-scale tracer tests suggest that the structure is consistent with a network of highly permeable sediments embedded in a less permeable matrix (Bianchi

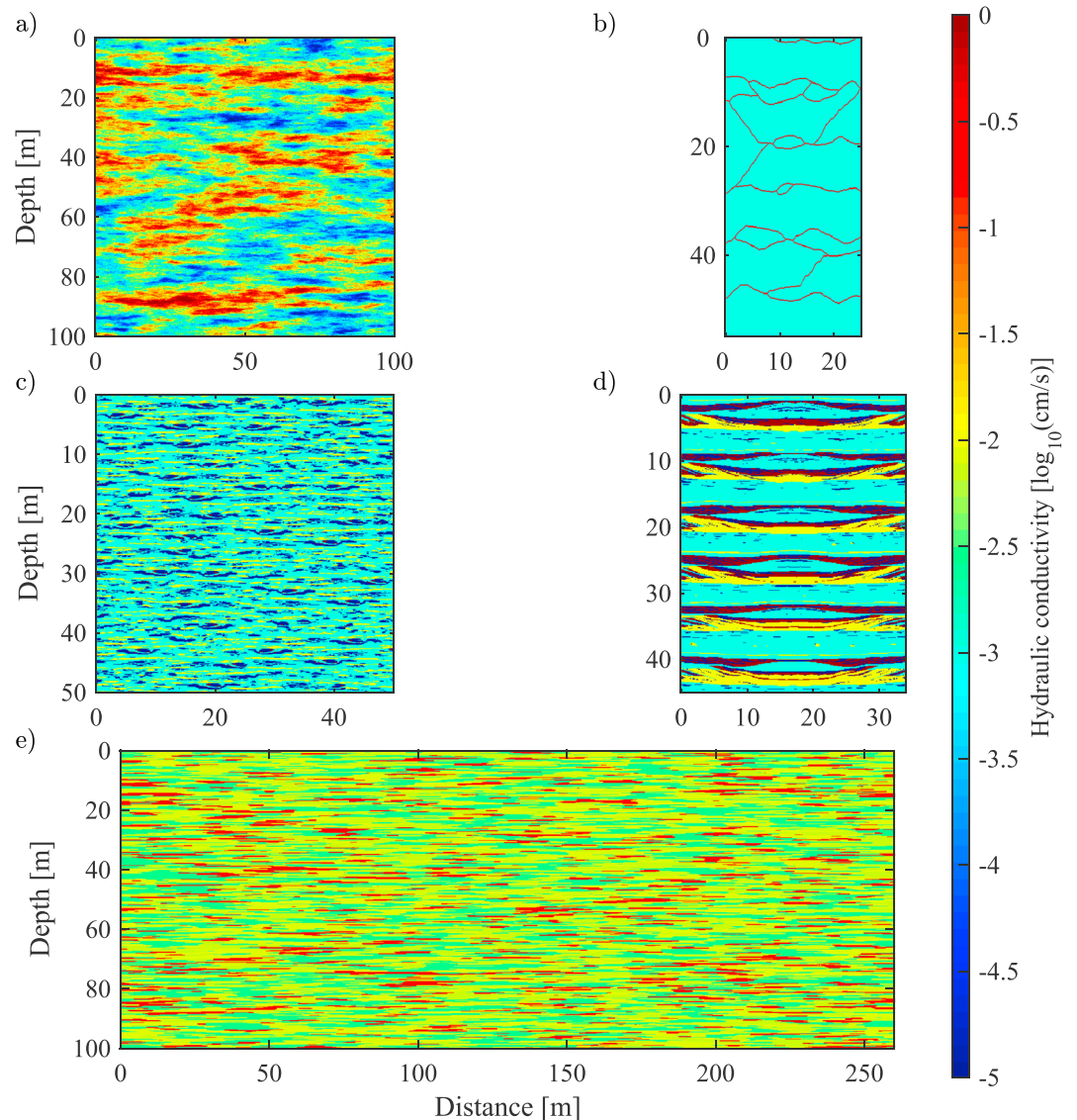


**Figure 2.** Training images used in the multiple-point statistics-based inversion to represent spatial hydraulic conductivity of the MADE site: (a) multi-Gaussian field (Bianchi, Zheng, Tick, et al., 2011), (b) highly conductive channels in a homogeneous matrix (Linde et al., 2015; Ronayne et al., 2010; Strebelle, 2002), (c) model based on a mapping study of a MADE outcrop (Linde et al., 2015; Rehfeldt et al., 1992), (d) model based on a mapping study at the Herten site in Germany (Bayer et al., 2011; Comunian et al., 2011; Linde et al., 2015) featuring representative alluvial deposit structures, and (e) model based on lithological borehole data collected at the MADE site (Bianchi & Zheng, 2016). MADE = MAcroDispersion Experiment.

& Zheng, 2016; Feehley et al., 2000; Harvey & Gorelick, 2000). The case study considered herein focuses on determining the most appropriate conceptual model of hydraulic conductivity in a reduced set given the multilevel solute concentration data collected during the MADE-5 tracer experiment (Bianchi, Zheng, Tick, et al., 2011). The test was performed in an array of four aligned boreholes with a maximum separation of 6 m. The concentration data used in this work were collected in the two inner multilevel sampler (MLS) wells between the outer injection and abstraction wells, which were screened over the entire aquifer thickness. Before tracer injection, a steady-state dipole flow field was established by injecting clean water. Then, a known volume of bromide solution was injected along the entire vertical profile of the aquifer for 366 min followed by continuous injection of clean water for 32 days. The flow rates at both the injection and extraction wells were kept practically constant during all the steps of the test. Bromide concentrations in the MLS wells were recorded at 19 different times and at seven depth levels (sampling ports) in each of the two MLS

**Table 1**  
*Geostatistical Parameters of the Multi-Gaussian Training Image (Figure 2a) Proposed by Bianchi, Zheng, Tick, et al. (2011) for the MADE Site*

Variogram parameters	Variogram model	
	Spherical	Exponential
Maximum range (m)	76	21
Minimum range (m)	4.6	5
Nugget	0.2	—
Sill	1.75	3.0

*Note.* The actual variogram model was a linear combination of a spherical and an exponential model. MADE = MAcroDispersion Experiment.

wells resulting in 266 concentration measurements. Full technical details about the experiment can be found in Bianchi, Zheng, Tick, et al. (2011). Given the particular design of the borehole array, groundwater flow and bromide tracer transport could be simulated only along the 2-D transect intercepting the four wells (the forward model used is described in Appendix A). This was necessary to reduce the computational demands in this application of the proposed Bayesian model selection method. In practice, the 2-D model assumes that the concentrations measured at the inner MLS wells are mainly the result of transport along straight flow paths between the injection and the abstraction wells. To enable such 2-D modeling, we performed a simple 3-D-to-2-D transformation of the data as described in Appendix A.

### 3.3.1. Conceptual Models at the MADE Site and Corresponding Training Images

We consider five training images that may represent spatially distributed hydraulic conductivity fields at the MADE site (Figure 2). The multi-Gaussian training image in Figure 2a was created as a 2-D unconditional realization obtained with the Sequential Gaussian SIMulation algorithm of the Stanford Geostatistical Modeling Software (Remy et al., 2009). The corresponding variogram parameters (Table 1) were calculated by Bianchi, Zheng, Tick, et al. (2011) from the analysis of more than 1,000 hydraulic conductivity values estimated by means of borehole flowmeter tests (Rehfeldt et al., 1992). According to Bianchi, Zheng, Tick, et al. (2011), the mean and variance in  $\log_{10}(\text{cm/s})$  is set equal to  $-2.37$  and  $1.95$ , respectively.

The training images in Figures 2b–2d were generated following Linde, Lochbühler, et al. (2015). The highly conductive and connected channels in an homogeneous matrix (Figure 2b) is built from the original training image of Strebelle (2002) modified according to the channel properties proposed by Ronayne et al. (2010) for the MADE site. The channel hydraulic conductivity is equal to  $-0.54$  in  $\log_{10}(\text{cm/s})$ , the channel thickness is  $0.2$  m, and the channel fraction is  $3.25\%$ . The training image in Figure 2c is based on hydrogeological facies, and their hydraulic conductivity values correspond to those of an outcrop located near the MADE site (Rehfeldt et al., 1992) and reported in Table 2.

The training image in Figure 2d is chosen solely on the knowledge that the aquifer at the MADE site is constituted by alluvial deposits (Boggs et al., 1992). Linde, Lochbühler, et al. (2015) and Lochbühler et al. (2014) used the training image of Figure 2d as derived from a detailed mapping study at the Herten site in Germany (Bayer et al., 2011; Comunian et al., 2011) featuring representative alluvial deposit structures and adapted it to the hydrogeological facies observed at the MADE site (Table 2).

**Table 2**  
*Hydrogeological Facies and Their Hydraulic Conductivity Values (Rehfeldt et al., 1992) Observed at the MADE Site Outcrop and Used for the Training Images in Figures 2c and 2d*

Facies	$\log_{10} K$ (cm/s)
Open framework gravel	$-6.83 \cdot 10^{-4}$
Sand	$-2.00$
Undifferentiated sandy gravel	$-3.00$
Sandy, clayey gravel	$-5.00$

**Table 3**  
*Hydrogeological Facies and Their Hydraulic Conductivity Values Based on Lithological Data From the MADE Site (Bianchi & Zheng, 2016) and Used for the Training Image in Figure 2e*

Facies	$\log_{10} K$ (cm/s)
Highly conductive gravel	-0.45
Sand and gravel	-2.05
Gravel with sand	-2.11
Well-sorted sand	-2.18
Sand gravel and fines	-2.53

Note. MADE = MAcroDispersion Experiment.

The training image of Figure 2e is built based on five hydrogeological facies identified from lithological borehole data at the MADE site (Bianchi & Zheng, 2016) and reported in Table 3. This training image is a stochastic unconditional realization that was generated following Bianchi and Zheng (2016).

Training images should be stationary and approach ergodicity (Caers & Zhang, 2004). This implies that the type of patterns found should not change over the domain covered by the training image (stationarity). Moreover, the size of the training image should be sufficiently large (at least double) compared to the largest pattern to enable adequate simulations (ergodicity). Small training images lead to large ergodic fluctuations that deteriorate pattern reproduction (Renard et al., 2005). Note that the smallest training image considered herein (Figure 2b) is 4 times wider than the size of the model domain in the horizontal direction.

In this work, we compare the five conceptual models of hydraulic conductivity that, in the following, we refer to as (1) *multi-Gaussian* as built from the training image in Figure 2a; (2) *hybrid* that consists of the highly conductive channels of Figure 2b overlaid on the multi-Gaussian background of Figure 2a; (3) *outcrop-based* built from the training image in Figure 2c; (4) *analog-based* built from the training image in Figure 2d; and (5) *lithofacies-based* built from the training image in Figure 2e. This selection of conceptual models allows us to compare very different parameterizations of the spatial heterogeneity at the MADE site. Note that a full assessment of all conceptual models that has been published for the MADE site is outside the scope of this study. Since computational limitations prohibit full 3-D simulations, we acknowledge that our findings in terms of the suitability of different conceptual models at the MADE site should be treated with some caution. Instead, the focus is on a new versatile methodology that enables comparison of widely different conceptual models.

### 3.4. Evidence Estimation in Practice

We discretize the power coefficients  $\beta$  using the commonly used power law of equation (16) (Baele & Lemey, 2013; Calderhead & Girolami, 2009; Friel & Pettitt, 2008a; Grzegorzczak et al., 2017; Höhna et al., 2017; Xie et al., 2011). According to these studies, the parameter  $c$  should be set equal to 3 or 5 and  $J$  as large as possible with the common choice of  $20 \leq J \leq 100$ . In this study, we chose  $c = 5$  and  $J = 40$ . For each  $\beta$  value, we run one MCMC chain of  $10^5$  iterations. These choices are dictated by computational constraints. The most challenging power posterior to sample is for  $\beta = 1$ , for which we run three chains to better explore the posterior distribution. Consequently, we run 42 MCMC chains for each conceptual model. Given that the log likelihoods obtained from the MCMC simulations are the basis for evidence estimations by power posteriors, we define the burn-in period (i.e., number of MCMC iterations required before reaching the target distribution) by considering the evolution of the log likelihoods. To assess when the log likelihood values start to oscillate around a constant value, we apply the Geweke method (Geweke, 1992) on the log likelihoods of each chain. This diagnostic compares the mean computed on the last half of the considered chain length against the one derived from a smaller interval in the beginning of the chain (in our case, 20% of the chain length). At first, the Geweke's method is applied to the whole chain (no burn-in), and if its statistics is outside the 95% confidence interval of the standard normal distribution, we apply it again after discarding the first 1%, 2%, ..., 95% of the total chain length. The burn-in is determined in this way for  $\beta = 1$ , as this is the most challenging case for which burn-in takes the longest time to achieve. The evidence estimates are computed using the thermodynamic integration method based on both the corrected trapezoidal rule (equation (7)), as well as with the stepping-stone sampling method (equation (14)). In order to correctly estimate the uncertainty of the evidence estimates, the effective sample size (equation (8)) in

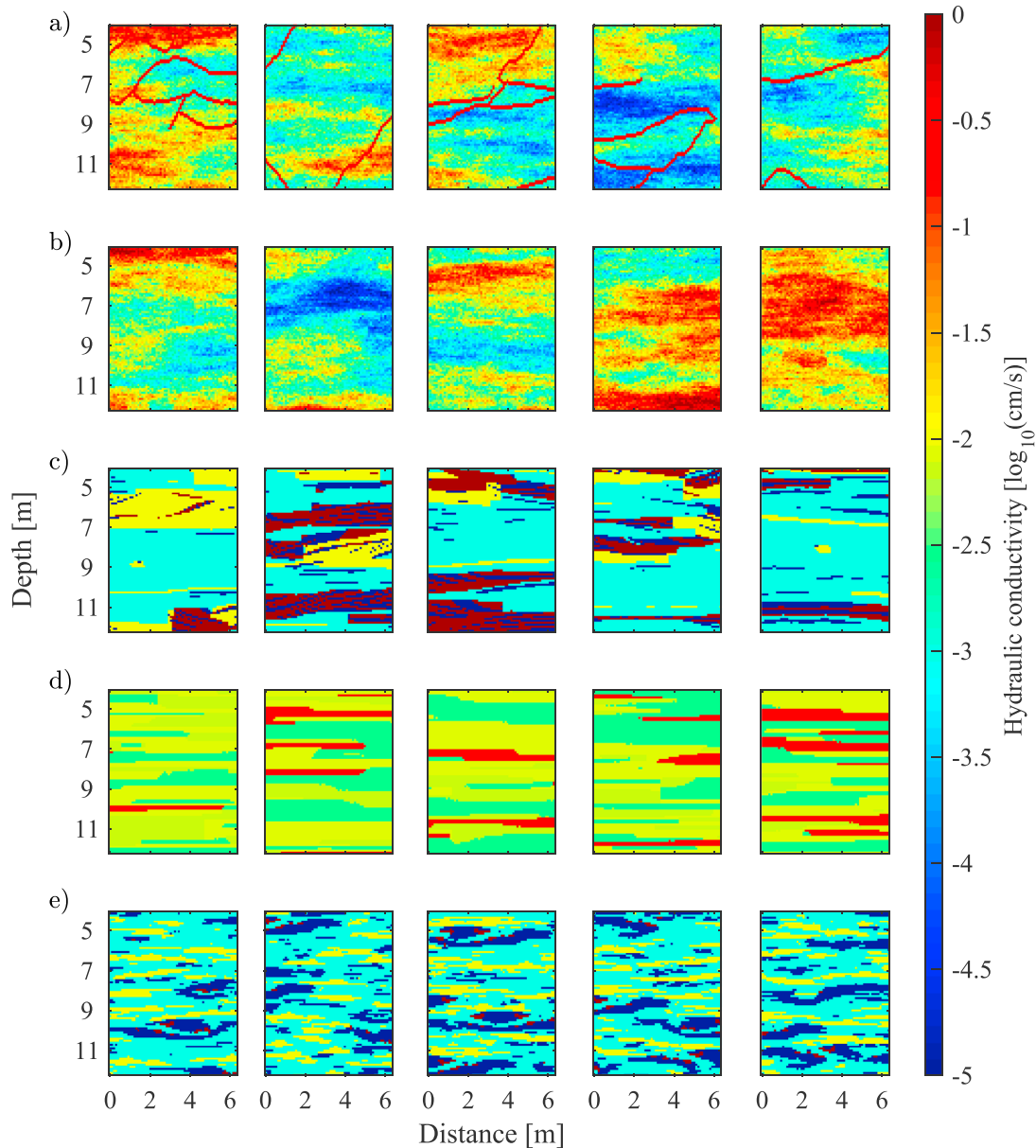


**Figure 3.** Five prior realizations of hydraulic conductivity fields generated from the training images of Figure 2 with the Graph Cuts algorithm for the (a) hybrid, (b) multi-Gaussian, (c) analog-based, (d) lithofacies-based, and (e) outcrop-based conceptual model of the MADE site. MADE = MACroDispersion Experiment.

each chain needs to be assessed. When evaluating equation (8), we truncate the sum in the denominator at the lag at which  $\rho_j(z)$  is within 95% confidence interval of the normal distribution with standard deviation equal to the standard error of the sample autocorrelation. The evidence estimates are updated continuously after burn-in to visualize their evolution with the number of MCMC iterations. The uncertainty associated with the evidence estimates are summarized by standard errors,  $SE = \sqrt{\hat{\text{Var}} \log p(\tilde{\mathbf{Y}}|\eta)}$  with corresponding 95% confidence intervals. The variances  $\hat{\text{Var}} \log p(\tilde{\mathbf{Y}}|\eta)$  are computed using equations (9) and (10) for the thermodynamic integration and using equation (15) for the stepping-stone sampling method.

## 4. Results for the MADE-5 Case Study

### 4.1. Bayesian Inference

For each of the conceptual models considered, we first show prior MPS realizations (i.e.,  $\beta = 0$ ) of hydraulic conductivity fields that are generated with the Graph Cuts method (Figure 3). Each set of prior realizations

**Table 4**  
Summary of MCMC Results Using the MADE-5 Tracer Data for Three MCMC Chains of  $10^5$  Steps for Each Conceptual Model With  $\beta = 1$

Conceptual model	AR (%)	Burn-in (%)			$\sigma_{\tilde{y}}$ (mg/L)	
		Chain 1	Chain 2	Chain 3	Mean	SD
Hybrid	0.6	—	58	87	5.81	0.27
Multi-Gaussian	8.0	48	45	62	7.14	0.33
Analog	4.1	—	64	84	7.22	0.34
Lithofacies	1.2	55	38	74	8.92	0.60
Outcrop	5.5	76	97	—	9.36	0.35

*Note.* First column, conceptual model considered; second column, average acceptance rate (AR); third to fifth columns, burn-in percentage based on the Geweke method for each of the three chains (when no value is displayed, the chain failed to reach burn-in); sixth and seventh columns, means and standard deviations of the measurement errors inferred with MCMC. MCMC = Markov chain Monte Carlo; MADE = MAcroDispersion Experiment.

shows considerable spatial variability and is in broad agreement with the original training image (Figure 2). This is valid for continuous (Figure 3b), categorical (Figures 3c–3e), and hybrid conceptual models (Figure 3a).

The posterior distributions (i.e.,  $\beta = 1$ ) are obtained by assuming that the standard deviation of the measurement errors,  $\sigma_{\tilde{y}}$  (mg/L), follows a log-uniform prior distribution in the range [1,10] mg/L (seventh column of Table 4). The lowest mean of the inferred  $\sigma_{\tilde{y}}$  is obtained for the hybrid conceptual model (5.8 mg/L) suggesting that this model enables the best match with the data. The highest  $\sigma_{\tilde{y}}$  is found for the outcrop-based model (9.4 mg/L). The acceptance rates are lower (second column in Table 4) than the ideal range between 15% and 40% proposed by Gelman et al. (1996), which suggests a slow convergence of the Markov chains. The burn-in time for each chain is obtained by the Geweke method (Table 4) as described in section 3.4.

The different conceptual models provide quite different posterior distributions of the hydraulic conductivity field (Figure 4), even if certain commonalities are observed. For instance, all the posterior models have a high-conductive zone at a depth of 7 m that extends to a depth of 8 m on the right-hand side of the model domain. These features are visible in both the posterior mean and the maximum a posteriori fields (first and second columns of Figure 4). The analog- and outcrop-based conceptual models exhibit more variability in the inferred hydraulic conductivity values (Figures 4c and 4e) with respect to the others, and the lithofacies-based conceptual model is characterized by the smallest posterior standard deviations (Figure 4d). The Gelman-Rubin statistic (Gelman & Rubin, 1992) is commonly used to assess if the MCMC chains have adequately sampled the posterior distribution, which is generally considered to be the case if this statistic is below 1.2. We see in the fourth column of Figure 4 that this is not the case for all pixel values, especially in the high-conductivity region, and that a larger number of iterations is required for a full convergence. However, we note that the evidence estimates are valid as long as the MCMC chains reach burn-in, while enhanced sampling decreases the estimation error.

In Figure 5, we show some of the simulated and observed breakthrough curves. We have chosen the ones at a depth of 7 m in the monitoring wells MLS-1 (Figure 5a) and MLS-2 (Figure 5b) because they correspond to a region of high conductivity (high concentrations) and the ones at a depth of 11 m that correspond to low concentrations in MLS-1 (Figure 5c) and MLS-2 (Figure 5d). Note that the range of measured concentration values spans 2 orders of magnitude (Figure 5). In general, the outcrop-based conceptual model is the worst in reproducing the observed breakthrough curves, while the hybrid model is the best performing one; this is particularly clear in Figure 5d. Corresponding plots at all measurement locations are found in the supporting information. The Pearson correlation coefficients between the simulated posterior mean concentrations and the observed ones are 0.96 for the hybrid model, 0.94 for the multi-Gaussian and analog-based models, and 0.91 for the lithofacies- and outcrop-based models.

#### 4.2. Bayesian Model Selection

In this section, we present the estimated evidence values for each conceptual model considered. Overall, the evidence values obtained using stepping-stone sampling and thermodynamic integration based on the corrected trapezoidal rule are in good agreement with each other considering their 95% confidence intervals

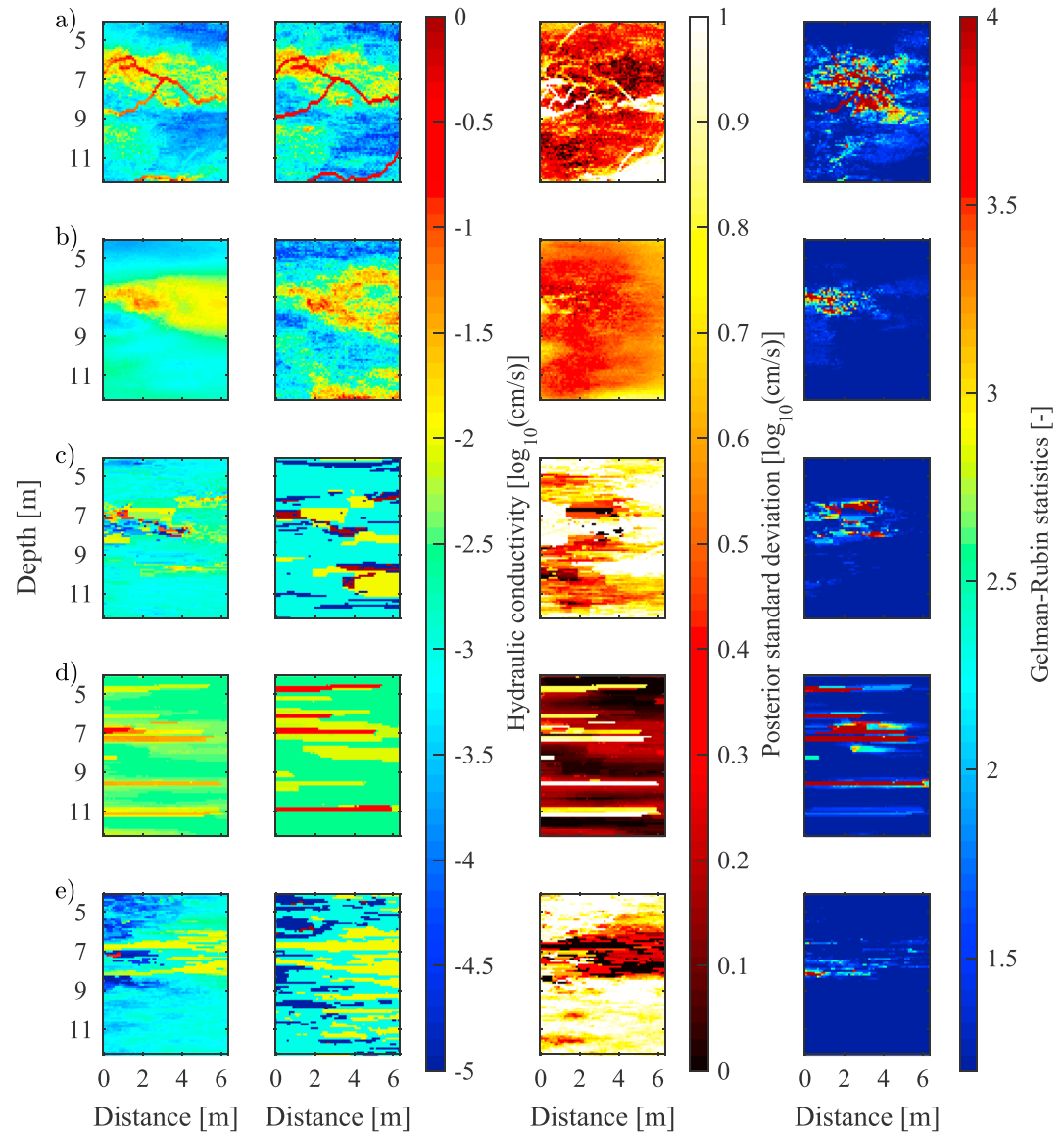


**Figure 4.** Mean (first column), maximum a posteriori (second column), and standard deviation (third column) of the posterior hydraulic conductivity realizations for the (a) hybrid, (b) multi-Gaussian, (c) analog-based, (d) lithofacies-based, and (e) outcrop-based conceptual model at the MADE site. In the fourth column, the Gelman-Rubin statistic for each pixel is reported. Dark blue regions represent values equal to or less than 1.2 and indicate that convergence has been reached for those pixels. MADE = MAcroDispersion Experiment.

(Figure 6). Moreover, except for some fluctuations at the early stage after burn-in, the evidence estimates evolve only slowly as a function of the number of MCMC iterations after burn-in (Figure 6). We find that stepping-stone sampling provides evidence values that are always lower than the ones estimated with the thermodynamic integration. This behavior is somewhat surprising as the stepping-stone sampling technique is not based on a discretization, while this is the case for thermodynamic integration leading to an expected underestimation of the evidence. The uncertainty associated with the stepping-stone evidence estimator decreases at a sustained pace when increasing the number of MCMC iterations, and it is lower than the one associated with thermodynamic integration (Figure 6 and Table 5). Thermodynamic integration is more affected by discretization errors, an error source that is independent of the number of MCMC iterations, than by sampling errors (Figure 8). For this reason, the width of the confidence intervals obtained by thermodynamic integration does not reduce significantly with increasing numbers of MCMC iterations (Figure 6).

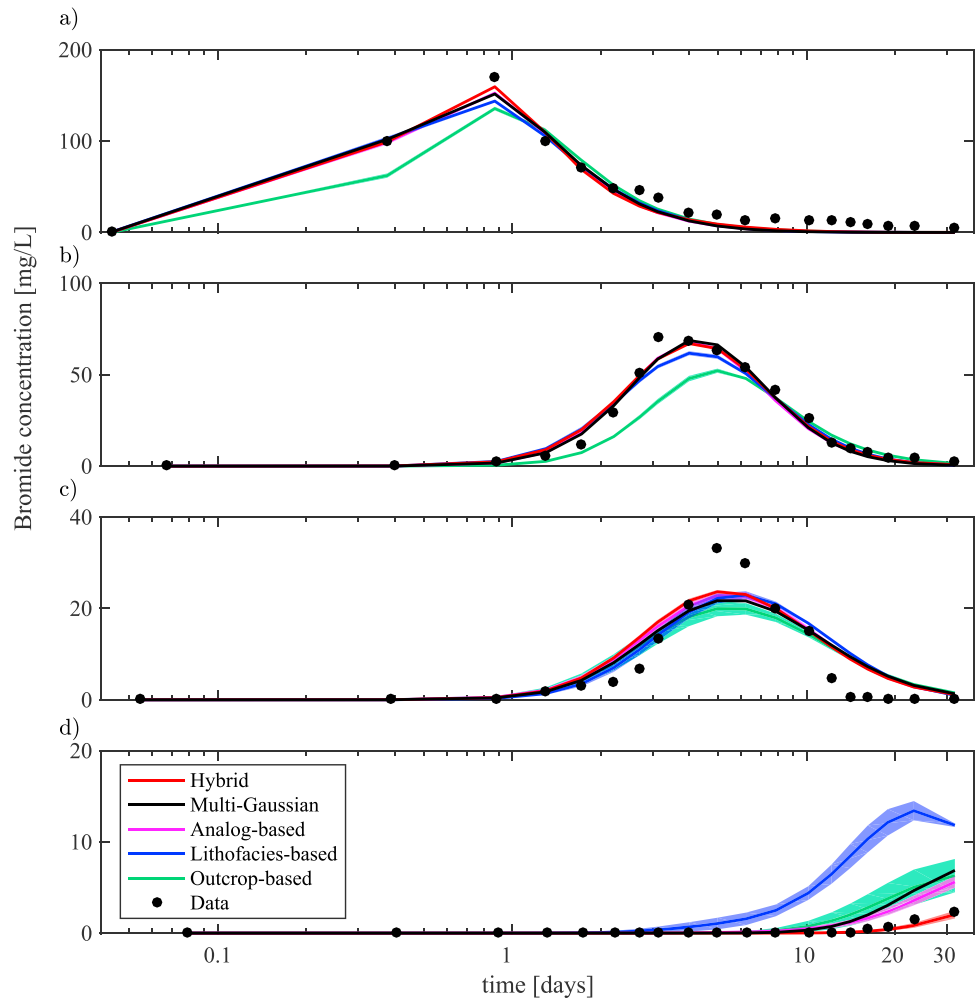


**Figure 5.** Simulated (solid lines) and measured (black dots) bromide breakthrough curves from the MAcroDispersion Experiment-5 experiment in the two monitoring wells MLS-1 and MLS-2 at depths of 7 m (a, b) and 11 m (c, d), respectively. The simulated breakthrough curves are summarized by the mean of the posterior realizations (solid lines) and their 95% confidence intervals (shaded areas). MLS = multilevel sampler.

Both evidence estimators lead to the same ranking of the conceptual models with the hybrid conceptual model having the largest evidence and the outcrop-based conceptual model having the lowest one (Table 5). The multi-Gaussian and the analog-based conceptual models have very similar evidence estimates, and they are the second-best performing conceptual models (Table 5).

For each conceptual model, the means of the log likelihood functions,  $\ell$ , increase with increasing  $\beta$  as we move from sampling the prior distribution ( $\beta = 0$ ) to sampling the posterior distribution ( $\beta = 1$ ; Figure 7). From  $\beta = 0$  to  $\beta = 0.1$ , the  $\ell$  estimates span 3 orders of magnitude. At very small values of  $\beta$  (i.e.,  $< 10^{-6}$ ), the outcrop-based conceptual model (green line in Figure 7) has mean log likelihoods that are almost 1 order of magnitude higher than the other models. With increasing  $\beta$ , the outcrop-based model shows a much less steep increase of  $\ell$ , and at  $\beta = 10^{-3}$ , they start to be lower than the log likelihood means of the other models. At higher power posteriors ( $\beta > 0.1$ ), the  $\ell$  estimates for the hybrid conceptual model are the highest (red line in Figure 7), which explains why the highest evidence value is found for the hybrid conceptual model. We also note that the mean log likelihood is not increasing continuously when  $\beta$  is close to 1, which we attribute to random fluctuations of the MCMC chains (Figure 7).

The percentage ratio of independent MCMC samples after burn-in is never above 10%, and it decreases to values as low as 0.01% for  $\beta = 1$  (Figure 8). This is a consequence of the slow mixing of the MCMC chains, and it explains the increase of the sampling errors with increasing  $\beta$  for both thermodynamic integration

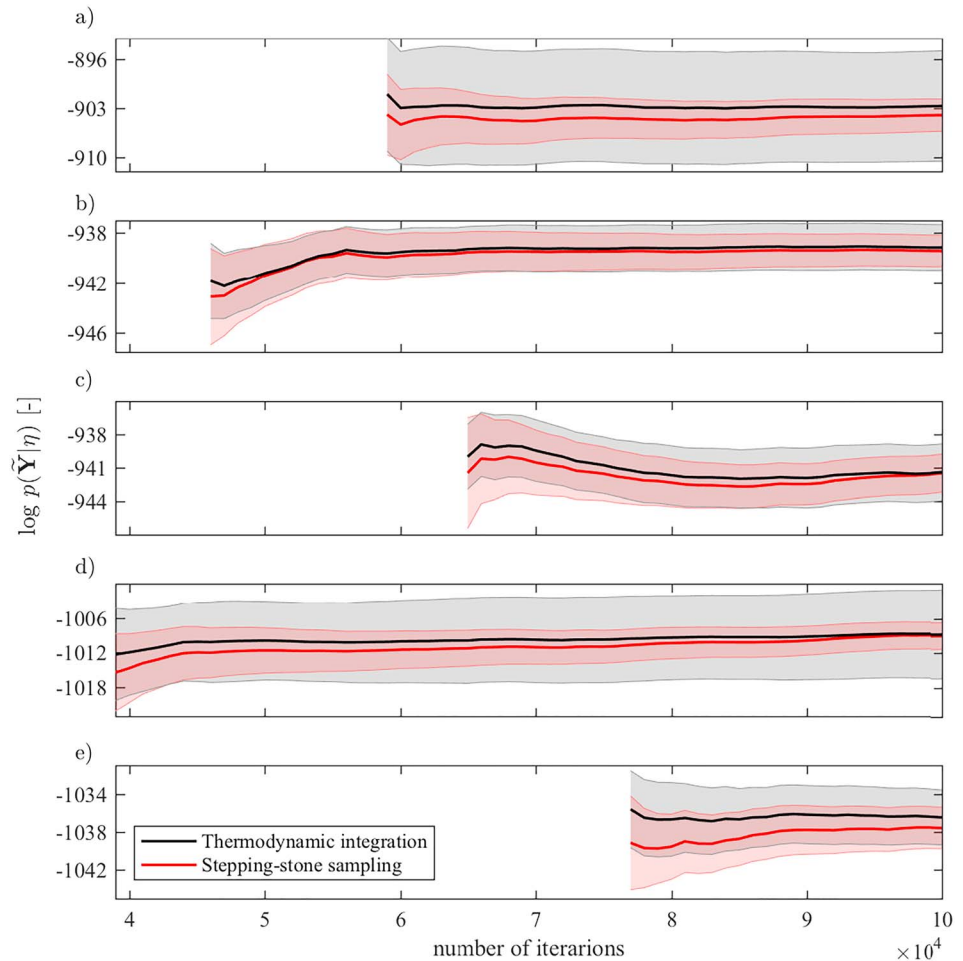


**Figure 6.** Natural logarithm of the evidence estimates,  $\log p(\tilde{Y}|\eta)$ , as a function of the number of MCMC iterations. Evidences are computed with the stepping-stone sampling method (red line) and the thermodynamic integration method based on the corrected trapezoidal rule (black line) for the (a) hybrid, (b) multi-Gaussian, (c) analog-based, (d) lithofacies-based, and (e) outcrop-based model at the MAcroDispersion Experiment site. The evidence computation starts after a different number of MCMC iterations because each of the conceptual models has a specific burn-in period. The shaded areas represent the 95% confidence interval of the evidence estimates (pink for stepping-stone sampling and grey for thermodynamic integration). MCMC = Markov chain Monte Carlo.

**Table 5**

*Estimates of the Natural Logarithm of the Evidence,  $\log p(\tilde{Y}|\eta)$ , With Corresponding Standard Errors, SE, for Each Conceptual Model (First Column) Based on the Stepping-Stone Sampling Method (Second and Third Columns) and on the Thermodynamic Integration Method With the Corrected Trapezoidal Rule (Fourth and Fifth Columns)*

Conceptual model	Stepping-stone sampling		Thermodynamic integration	
	$\log p(\tilde{Y} \eta)$ (-)	SE (-)	$\log p(\tilde{Y} \eta)$ (-)	SE (-)
Hybrid	-903.99	1.17	-902.68	4.02
Multi-Gaussian	-939.43	0.64	-939.15	0.93
Analog	-941.48	0.87	-941.40	1.30
Lithofacies	-1009.01	1.18	-1008.76	3.90
Outcrop	-1037.58	1.11	-1036.45	1.47

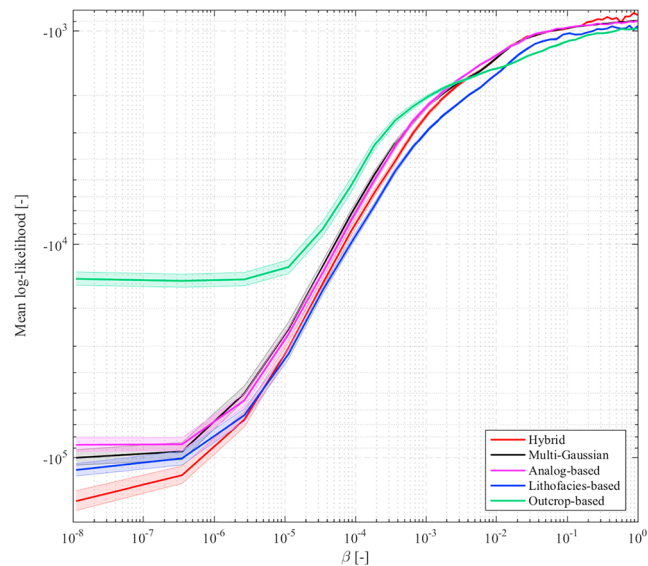


**Figure 7.** Mean (line) of the natural logarithm of the likelihood functions,  $\ell$ , computed for each  $\beta$  value and the 95% confidence interval of the  $\ell$  estimates (shaded areas). Note that the  $x$  and  $y$  axes are in  $\log_{10}$  scale.

(Figure 8c) and stepping-stone sampling (Figure 8d). The sampling errors of the stepping-stone sampling method are always at least 2 orders of magnitude higher than the ones related to the thermodynamic method, but this method is devoid of discretization errors, which constitutes the dominant error type for thermodynamic integration. As mentioned before, using a power law to distribute  $\beta$  values (equation (16)) ensures that the discretization errors for small  $\beta$  are relatively small (i.e., between  $10^{-10}$  and  $10^{-3}$ ; Figure 8b). The pronounced fluctuations of the discretization errors especially for  $\beta > 0.1$  (Figure 8b) are related to the fact that the mean of the log likelihoods does not increase monotonically for high  $\beta$  values.

We now compute the Bayes factors for the best conceptual model (hybrid) with respect to each of the other competing conceptual models. In particular, we follow the guideline proposed by Kass and Raftery (1995) and we present twice the natural logarithm of the Bayes factors (Figures 9a and 9b). The Bayes factors of the hybrid conceptual model are on the order of  $10^{15}$  and  $10^{16}$  relative to the second best models (multi-Gaussian and analog-based) and  $10^{58}$  relative to the worst model (outcrop-based) for both thermodynamic integration and stepping-stone sampling. Note that the measure of twice the natural logarithms of the Bayes factors are all larger than 50 (Figures 9a and 9b). According to the interpretation of Kass and Raftery (1995), we can safely claim that the hybrid model shows very strong evidence of being superior to the other considered conceptual models. The Bayes factors computed with the stepping-stone sampling method have smaller uncertainties (Figure 9b) than the ones based on thermodynamic integration (Figure 9a). We note that the relative rankings of the competing models obtained with the thermodynamic integration and the stepping-stone sampling methods are consistent and stable as long as the MCMC chains has reached burn-in. Practically, this suggests that we can perform and obtain reliable Bayesian model selection results at less computational cost and, again, that formal convergence of the MCMC chains is not necessary.

## 5. Discussion

We have proposed a new methodology targeted at Bayesian model selection among geologically realistic conceptual models that are represented by training images. For MCMC inversions, we use sequential geostatistical resampling through Graph Cuts that is 2 orders of magnitude faster than the forward simulation time (i.e., 0.08 vs. 8.35 s). In addition to being fast, the model realizations based on Graph Cuts are of high quality and honor the geological patterns in the training images. This is true for the five different types of conceptual models considered (Figures 3 and 4). Moreover, the Graph Cuts algorithm can include point conditioning (Li et al., 2016) even if this is not considered herein. In our 2-D analysis, we find that the hybrid conceptual model allows for the best fit of the observed breakthrough curves (Figure 5). The inclusion of highly conductive channels in a multi-Gaussian background enables enhanced simulations of the maximal concentrations, and it is in general agreement with the expected subsurface structure at the MADE site (i.e.,

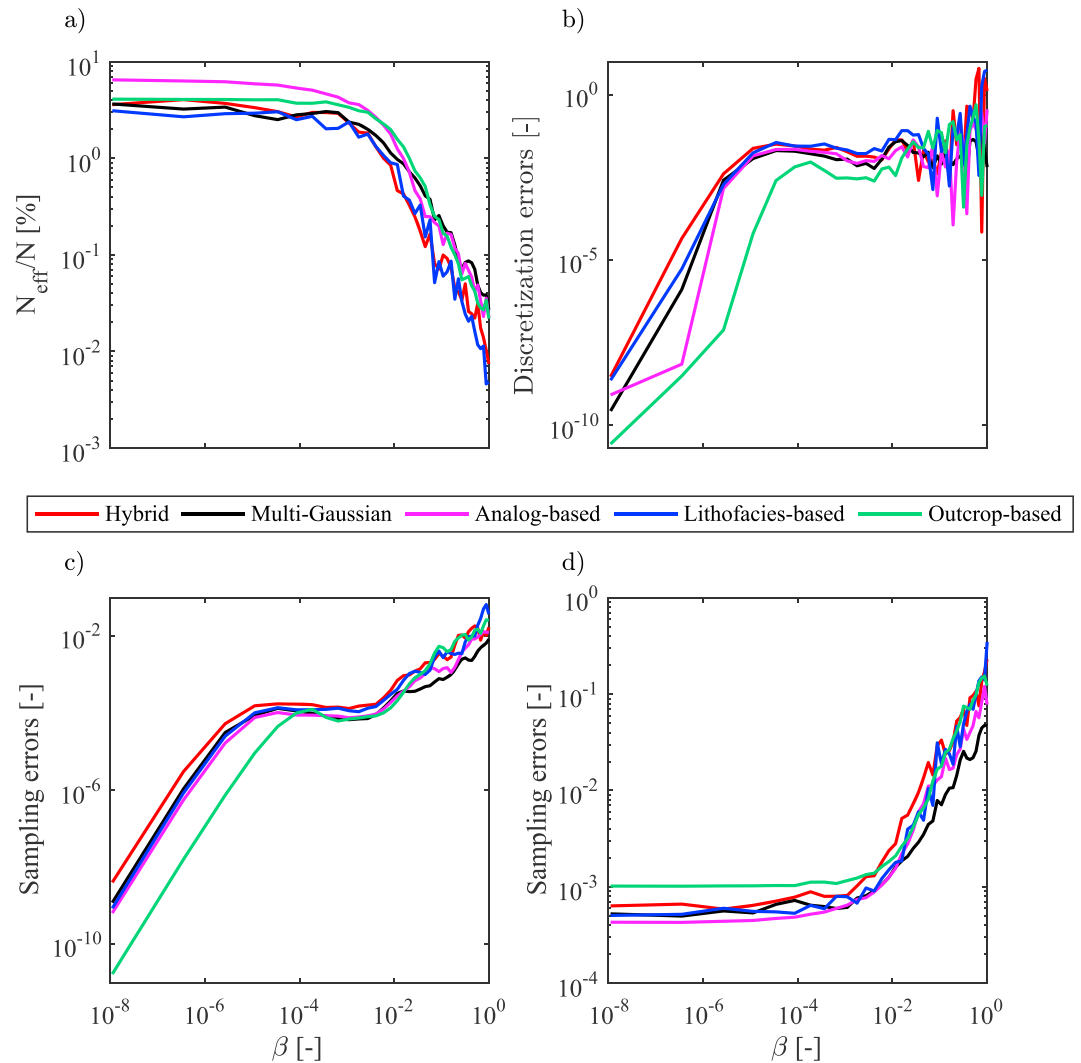


**Figure 8.** (a) Percentage ratio between the effective and the total number of Markov chain Monte Carlo samples, (b) discretization errors in the thermodynamic integration method (square root of equation (10)), (c) sampling errors in the thermodynamic integration method (square root of equation (9)), and (d) sampling errors in the stepping-stone sampling method (square root of equation (15)) as a function of  $\beta$  values. Note that all the  $x$  and  $y$  axes are in  $\log_{10}$  scale.

highly permeable network of sediments embedded in a less permeable matrix; Bianchi, Zheng, Tick, et al., 2011; Bianchi, Zheng, Wilson, et al., 2011; Harvey & Gorelick, 2000; Liu et al., 2010; Ronayne et al., 2010; Zheng & Gorelick, 2003). We find that the outcrop model has not enough degrees of freedom to properly fit the solute concentration data (Figure 5). Furthermore, we expect that an improved data fit would have been possible if we additionally would have inferred certain model parameter values (e.g., hydraulic conductivity for each facies and for the geostatistical parameters of the multi-Gaussian field).

In the light of the MADE-5 solute concentration data considered, the best fitting model (hybrid) is also the one that has the highest evidence, while the outcrop-based conceptual model has a Bayes factor of  $10^{-58}$  with respect to the hybrid one, the lowest evidence, and the lowest data fit (Table 4, Figure 6, and Table 5). Linde, Lochbühler, et al. (2015) rank different conceptual models (only the analog- and outcrop-based models are exactly the same as in the present work) of the region between the MLS-1 and MLS-2 wells using the maximum likelihood estimate based on geophysical data (cross-hole ground-penetrating radar data). In agreement with our results, Linde, Lochbühler, et al. (2015) find that the analog-based conceptual model explains the data much better than the outcrop-based conceptual model and that the latter is the worst performing one in the considered set.

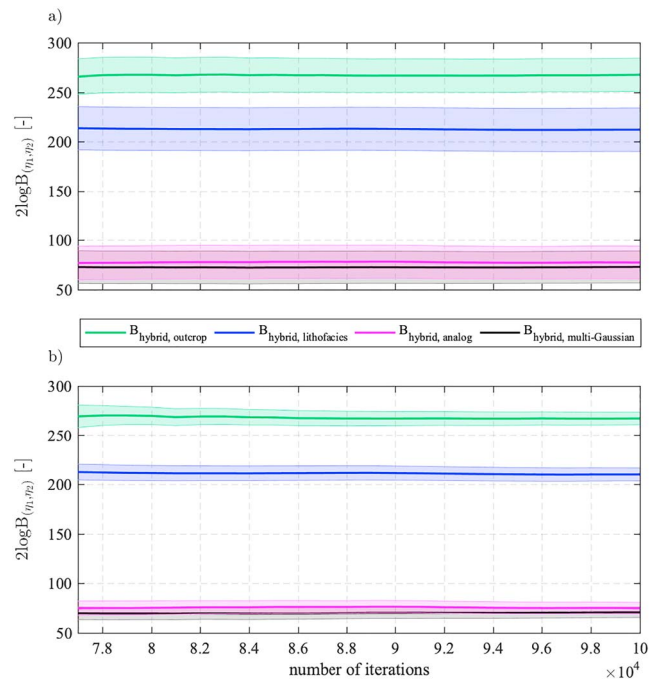


**Figure 9.** Twice the natural logarithm of the Bayes factors of the “best model” (hybrid) with respect to the outcrop-based (green line), lithofacies-based (blue line), analog-based (magenta line), and multi-Gaussian (black line) conceptual model at the MACroDispersion Experiment site. Results are shown for (a) the thermodynamic integration method based on the corrected trapezoidal rule and for the (b) stepping-stone sampling method. The shaded areas represent the 95% confidence interval of the  $2\log B_{\eta_1, \eta_2}$  measures.

Our results suggest that when comparing complex conceptual models represented by training images in data-rich environments, it may sometimes be possible to simply rank the performance of the competing conceptual models based on the inferred standard deviation of the measurement errors,  $\sigma_{\tilde{y}}$  (Table 4), or the maximum likelihood estimate. Similar results for more traditional spatial priors were also found in other studies (Brunetti et al., 2017; Schöniger et al., 2014). However, note that maximum likelihood-based model ranking will sometimes fail miserably as Bayesian model selection considers the trade-off between parsimony and goodness of fit. For instance, we expect that if we would have considered an uncorrelated hydraulic conductivity field, it would have produced the best fitting model but not the highest evidence. Moreover, it is also clear from these results that simply sampling the prior ( $\beta = 0$ ) and then ranking the competing conceptual models based on the mean of the sampled likelihoods may provide misleading results. Indeed, the outcrop-based model has mean likelihoods of the prior model that are almost 1 order of magnitude higher than the ones of the other models (Figure 7) and, therefore, such a ranking would suggest that the outcrop-based conceptual model is the best one in describing the data while it is actually the worst one.

We find that stepping-stone sampling almost always provides slightly lower evidence estimates than thermodynamic integration (Table 5). This is in disagreement with the theory and with results by Xie et al. (2011) and Friel et al. (2014). We attribute these unexpected results to the facts that (1) the MCMC chains for  $\beta$  close to 1 do not reach full convergence and the stepping-stone sampling is sensitive to poor convergence (Friel et al., 2014) and (2) most of the contribution to the total evidence estimate comes from the terms of equation (7) computed for  $\beta > 0.1$ , a region where the mean log likelihood does not increase monotonically due to random fluctuations of the MCMC chains (Figure 7). We also highlight that the comparison between the uncertainty estimates of the evidence values provided by thermodynamic integration and stepping-stone sampling (Figure 6) is not completely fair since the discretization errors affecting thermodynamic integration are based on a worst case scenario that arises from the approximation of equation (6) with a rectangular rule.

We stress again that our main intent is to present and demonstrate the proposed methodology targeted at Bayesian model selection among geologically realistic conceptual models. Computational constraints made it infeasible to perform model selection in 3-D. Instead, given the particular design of the tracer experiment

(i.e., array of four aligned boreholes), we used a 2-D flow and transport model, and the data were corrected using a 3-D-to-2-D transformation that accounts for differences in flow paths for a homogeneous subsurface (Appendix A). Since 3-D heterogeneity is important at the MADE site, our 2-D model ranking should only be considered approximate.

Future work should better account for model errors caused by the 3-D-to-2-D flow and transport approximation described in Appendix A. This would enhance the ability to make more definite statements about aquifer heterogeneity at the MADE site. How to properly account for and represent model errors is a challenging task especially in problems involving many data, high-dimensional parameter spaces, and nonlinear forward models (e.g., Linde et al., 2017). Another interesting topic that could be explored is to apply parallel tempering and use the resulting chains for computing the evidence with thermodynamic integration or stepping-stone sampling (Bailer-Jones, 2015; Earl & Deem, 2005; Vlugt & Smit, 2001). Parallel tempering allows swapping between chains and, thereby, improving sampling efficiency. This may contribute to more robust results, faster convergence and, thereby, increase the number of effective samples (Figure 8a).

## 6. Conclusions

Inversions with geologically realistic priors can be performed using training images and model proposals that honor their MPS. Unfortunately, such inversions cannot rely on many state-of-the-art inversion methods and associated approaches for calculating the evidence needed when performing Bayesian model selection. In this work, we introduce a new full Bayesian methodology to enable Bayesian model selection among complex geological priors. To demonstrate this methodology, we have evaluated its performance in the context of determining, in a reduced set, the conceptual model that best explains the concentration data for the case study considered (MADE-5). Our methodology is applicable to both continuous and categorical conceptual models (e.g., a geologic facies image), and it could be used at other sites and scales and for different data types. Thermodynamic integration and stepping-stone sampling methods are used for evidence computation using a series of power posteriors obtained from MPS-based inversions. They provide a consistent ranking of the competing conceptual models regardless of the number of MCMC iterations after burn-in. This suggests that one can perform and obtain reliable Bayesian model selection results with MCMC chains that have only achieved limited sampling after burn-in. Both thermodynamic integration and stepping stone sampling are suitable evidence estimators. However, we recommend the stepping-stone sampling method because it is not affected by discretization errors and its uncertainty (sampling errors) is significantly decreased with increasing numbers of MCMC iterations. This is not the case for the thermodynamic integration because it is affected by discretization errors that dominate over the sampling errors. From the power posteriors derived from the test case, we find that (1) ranking the conceptual models based on prior sampling only ( $\beta = 0$ ) favors the conceptual model with the lowest evidence and (2) model ranking based on the maximum posterior likelihood estimates ( $\beta = 1$ ) provides, for this specific example, the same results as the formal Bayesian model selection methods considered herein. For improved sampling, we suggest that future work should investigate the use of parallel tempering results for evidence computations. Moreover, a full 3-D analysis or a more formal treatment of model errors due to the considered 3-D-to-2-D approximation would enhance the confidence in statements about the suitability of alternative conceptual models at highly heterogeneous field sites.

## Appendix A: Forward Model: From 3-D to 2-D

The forward model used by Bianchi, Zheng, Tick, et al. (2011) to simulate the bromide concentrations during the MADE-5 experiment is a 3-D block-centered finite-difference model based on MODFLOW (3-D flow simulator; Harbaugh, 2005) and MT3DMS (3-D transport simulator; Zheng, 2010). We initially consider a fine spatial discretization of 0.1 m in the area around the wells (Figures A1a and A1b). However, running such a 3-D model is computationally prohibitive for evidence computations (i.e., 15 min of computing time to get one forward response and we need  $10^5$  forward evaluations for each MCMC chain and power posterior considered). To reduce the computing time, we perform a simple 3-D to 2-D correction of the data followed by 2-D flow and transport simulations using the finite-volume algorithm MaFloT (Künze & Lunati, 2012). Moreover, we restrict the simulations to the best fitting cross section (red segment in Figures A1a and A1b) between the positions of the injection, extraction, and the two MLS wells, which results in an area of 6.3 m  $\times$  8.1 m (Figure A1c). For the transport equation, we set Dirichlet boundary conditions with the normalized

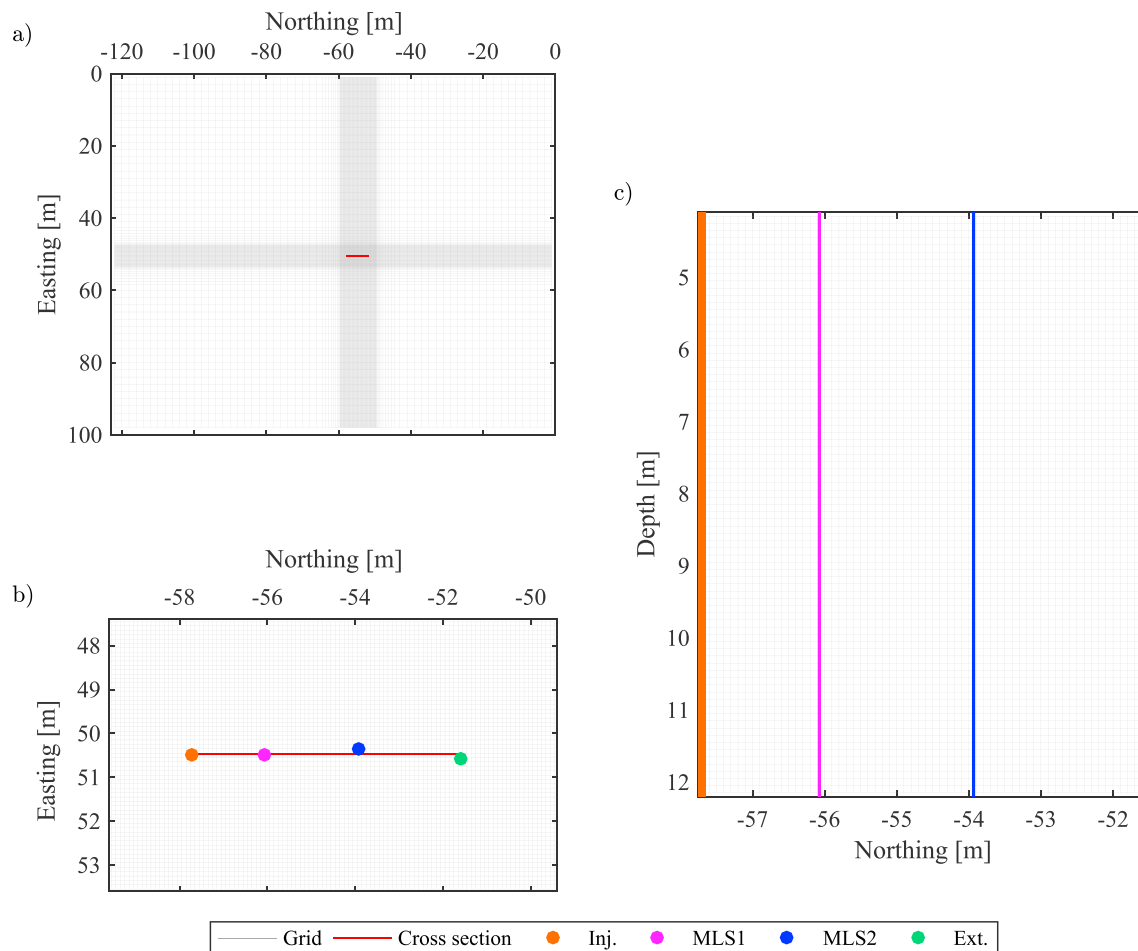


**Figure A1.** (a) Aerial view of the 3-D grid used for simulations with MODFLOW/MT3DMS; (b) zoom in the tracer test area, in which the grid size was refined to 0.1 m; (c) cross section used for simulations with MaFloT. The width of the lines in (c) is representative of the diameter of the four wells.

concentration to the given fluxes on the left side of the model domain (Figure A1c) corresponding to the injection well location. For the pressure equation, we set Dirichlet boundary conditions at the west and east sides (i.e., pressure difference) and Neumann boundary conditions at the north and south sides of the model domain (Figure A1c).

Formal approaches to account for model errors in MCMC inversions exist (e.g., Cui et al., 2011), but they are outside the scope of the present contribution. In the following, we introduce a simple error model that allows us to correct for the leading effects of the 3-D to 2-D transformation. These modeling errors stem primarily from the 2-D linear approximation of the 3-D radial distribution of the hydraulic heads, which results in a time shift in the breakthrough curves at the MLS wells. To estimate the correction factors, we consider a uniform hydraulic conductivity model with the geometric mean hydraulic conductivity at the MADE site (i.e.,  $4.3 \cdot 10^{-5}$  m/s; Rehfeldt et al., 1992). For this model, we perform 3-D and 2-D simulations of the MADE-5 experiment with MODFLOW/MT3DMS and MaFloT, respectively. As expected, the 3-D simulated hydraulic heads between the injection and extraction wells do not change linearly as for the 2-D simulation (Figure A2). We tune the injection rate in the MODFLOW simulations to achieve simulated hydraulic heads that are as close as possible to the measured ones. We then perform MaFloT simulations using the MODFLOW simulated hydraulic heads at the injection and extraction wells as boundary conditions, and we compute correction factors at the MLS wells. These multiplicative correction factors are those that maximize the correlation between the concentrations simulated with MT3DMS and MaFloT. The mean correction factors over the seven sampling ports in each of the two MLS wells are 1.09 and 1.92. Once the correction factors have been applied, the earlier time shifts (Figures A2b and A2c) are removed (Figures A2d and A2e). These correction factors are used in all subsequent simulations. Note that no attempt is made to correct for

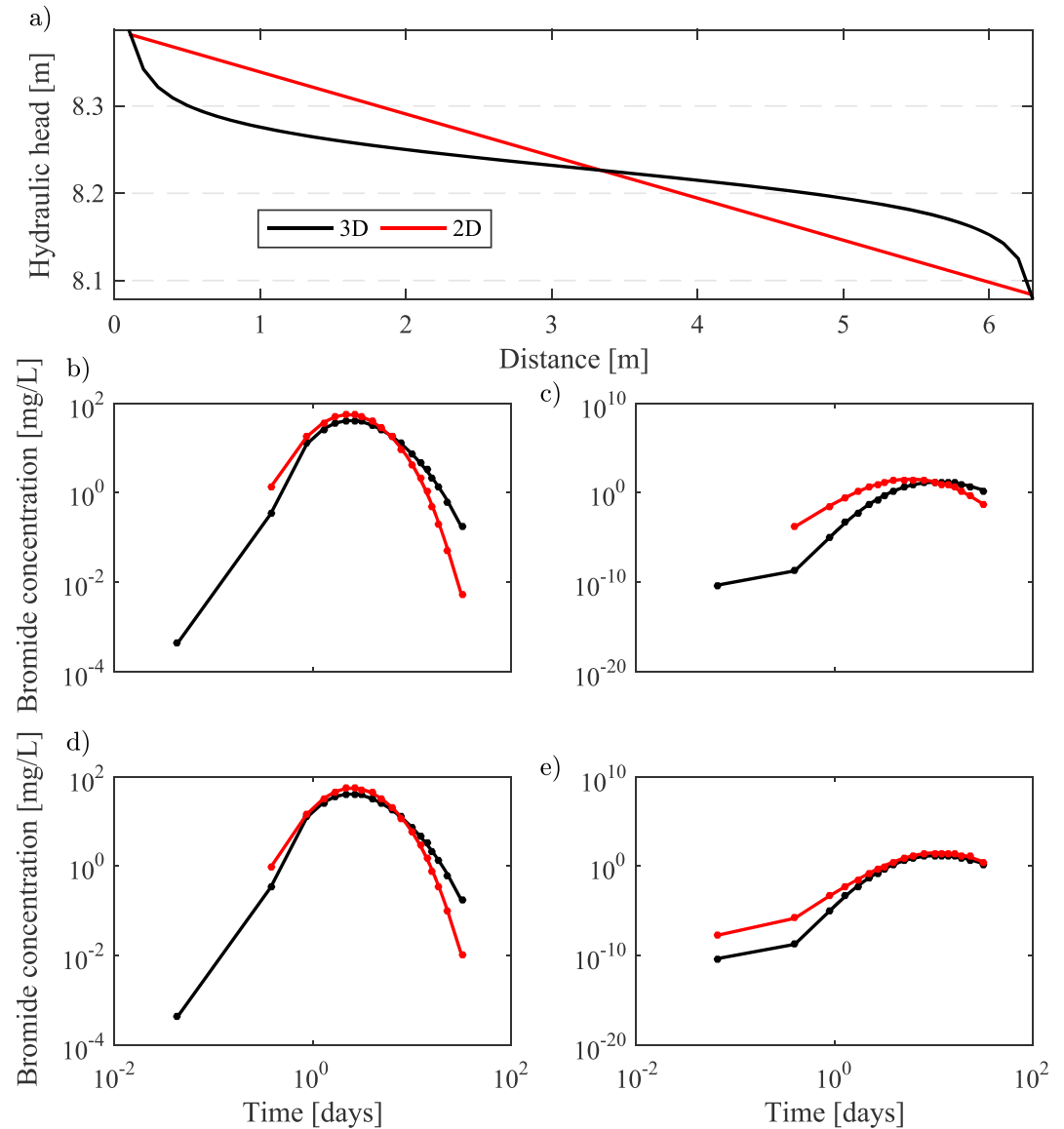


**Figure A2.** (a) Hydraulic head profiles between the injection and extraction wells arising from 2-D and 3-D flow simulations in a uniform hydraulic conductivity field. Simulated breakthrough curves at 7-m depth in (b) MLS-1 and (c) MLS-2 without corrections. The shifts in the 2-D simulations are removed when (d, e) applying the correction factors. MLS = multilevel sampler.

tracer movement due to 3-D heterogeneity; the correction is a simple geometrical correction to account for the transformation of a uniform 3-D to 2-D flow field. We acknowledge that this is a crude approximation, but we deem it sufficient for the purposes of the present paper.

## References

- Baele, G., & Lemey, P. (2013). Bayesian evolutionary model testing in the phylogenomics era: Matching model complexity with computational efficiency. *Bioinformatics*, 29(16), 1970–1979. <https://doi.org/10.1093/bioinformatics/btt340>
- Baele, G., Lemey, P., & Vansteelandt, S. (2013). Make the most of your samples: Bayes factor estimators for high-dimensional models of sequence evolution. *BMC bioinformatics*, 14(1), 85. <https://doi.org/10.1186/1471-2105-14-85>
- Bailer-Jones, C. A. (2015). A general method for Bayesian time series modelling (*Tech rep.*) Heidelberg: Max Planck Institute for Astronomy.
- Bayer, P., Huggenberger, P., Renard, P., & Comunian, A. (2011). Three-dimensional high resolution fluvio-glacial aquifer analog: Part 1: Field study. *Journal of Hydrology*, 405(1-2), 1–9. <https://doi.org/10.1016/j.jhydrol.2011.03.038>
- Bazargan, H., & Christie, M. (2017). Bayesian model selection for complex geological structures using polynomial chaos proxy. *Computational Geosciences*, 21(3), 533–551. <https://doi.org/10.1007/s10596-017-9629-0>

## Acknowledgments

This work was supported by the Swiss National Science Foundation under grant 200021\_155924. Niklas Linde thanks Arnaud Doucet for initially suggesting the use of thermodynamic integration. Marco Bianchi publishes with the permission of the Executive Director of the British Geological Survey. The training images are available at <https://doi.org/10.5281/zenodo.2545587>, and the concentration data of the MADE-5 tracer experiment will be soon available at the website (<https://www.bgs.ac.uk/services/NGDC/>).

- Bianchi, M., & Zheng, C. (2016). A lithofacies approach for modeling non-Fickian solute transport in a heterogeneous alluvial aquifer. *Water Resources Research*, *52*, 552–565. <https://doi.org/10.1002/2015WR018186>
- Bianchi, M., Zheng, C., Tick, G. R., & Gorelick, S. M. (2011). Investigation of small-scale preferential flow with a forced-gradient tracer test. *Groundwater*, *49*(4), 503–514. <https://doi.org/10.1111/j.1745-6584.2010.00746.x>
- Bianchi, M., Zheng, C., Wilson, C., Tick, G. R., Liu, G., & Gorelick, S. M. (2011). Spatial connectivity in a highly heterogeneous aquifer: From cores to preferential flow paths. *Water Resources Research*, *47*, W05524. <https://doi.org/10.1029/2009WR008966>
- Boggs, J. M., Young, S. C., Beard, L. M., Gelhar, L. W., Rehfeldt, K. R., & Adams, E. E. (1992). Field study of dispersion in a heterogeneous aquifer: 1. Overview and site description. *Water Resources Research*, *28*(12), 3281–3291. <https://doi.org/10.1029/92WR01756>
- Bond, C. E., Gibbs, A. D., Shipton, Z. K., & Jones, S. (2007). What do you think this is? “Conceptual uncertainty” in geoscience interpretation. *GSA today*, *17*(11), 4. <https://doi.org/10.1130/GSAT01711A.1>
- Boykov, Y., & Kolmogorov, V. (2004). An experimental comparison of min-cut/max-flow algorithms for energy minimization in vision. *IEEE Transactions on Pattern Analysis and Machine Intelligence*, *26*(9), 1124–1137. <https://doi.org/10.1109/TPAMI.2004.60>
- Brunetti, C., Linde, N., & Vrugt, J. A. (2017). Bayesian model selection in hydrogeophysics: Application to conceptual subsurface models of the South Oyster Bacterial Transport Site, Virginia, USA. *Advances in Water Resources*, *102*, 127–141. <https://doi.org/10.1016/j.advwatres.2017.02.006>
- Caers, J., & Zhang, T. (2004). Multiple-point geostatistics: A quantitative vehicle for integrating geologic analogs into multiple reservoir models. In G. M. Grammer, P. M. Harris, & G. P. Eberli (Eds.), *Chap. 18 Integration of outcrop and modern analogs in reservoir modeling* (pp. 383–394). California, USA: American Association of Petroleum Geologists. <https://doi.org/10.1306/M80924C18>
- Calderhead, B., & Girolami, M. (2009). Estimating Bayes factors via thermodynamic integration and population MCMC. *Computational Statistics & Data Analysis*, *53*(12), 4028–4045. <https://doi.org/10.1016/j.csda.2009.07.025>
- Cao, T., Zeng, X., Wu, J., Wang, D., Sun, Y., Zhu, X., et al. (2018). Integrating MT-DREAMzs and nested sampling algorithms to estimate marginal likelihood and comparison with several other methods. *Journal of Hydrology*, *563*, 750–765. <https://doi.org/10.1016/j.jhydrol.2018.06.055>
- Comunian, A., Renard, P., Straubhaar, J., & Bayer, P. (2011). Three-dimensional high resolution fluvio-glacial aquifer analog: Part 2: Geostatistical modeling. *Journal of hydrology*, *405*(1–2), 10–23. <https://doi.org/10.1016/j.jhydrol.2011.03.037>
- Cui, T., Fox, C., & O'sullivan, M. (2011). Bayesian calibration of a large-scale geothermal reservoir model by a new adaptive delayed acceptance Metropolis Hastings algorithm. *Water Resources Research*, *47*, W10521. <https://doi.org/10.1029/2010WR010352>
- De Marsily, G., Delay, F., Gonçalves, J., Renard, P., Teles, V., & Violette, S. (2005). Dealing with spatial heterogeneity. *Hydrogeology Journal*, *13*(1), 161–183. <https://doi.org/10.1007/s10040-004-0432-3>
- Dettmer, J., Dosso, S. E., & Osler, J. C. (2010). Bayesian evidence computation for model selection in non-linear geoaoustic inference problems. *Journal of the Acoustical Society of America*, *128*(6), 3406–3415. <https://doi.org/10.1121/1.3506345>
- Earl, D. J., & Deem, M. W. (2005). Parallel tempering: Theory, applications, and new perspectives. *Physical Chemistry Chemical Physics*, *7*(23), 3910–3916. <https://doi.org/10.1039/B509983H>
- Elsheikh, A. H., Demyanov, V., Tavakoli, R., Christie, M. A., & Wheeler, M. F. (2015). Calibration of channelized subsurface flow models using nested sampling and soft probabilities. *Advances in Water Resources*, *75*, 14–30. <https://doi.org/10.1016/j.advwatres.2014.10.006>
- Fan, Y., Wu, R., Chen, M.-H., Kuo, L., & Lewis, P. O. (2011). Choosing among partition models in Bayesian phylogenetics. *Molecular biology and evolution*, *28*(1), 523–532. <https://doi.org/10.1093/molbev/msq224>
- Feehley, C. E., Zheng, C., & Molz, F. J. (2000). A dual-domain mass transfer approach for modeling solute transport in heterogeneous aquifers: Application to the Macrodispersion Experiment (MADE) site. *Water Resources Research*, *36*(9), 2501–2515. <https://doi.org/10.1029/2000WR900148>
- Friel, N., Hurn, M., & Wyse, J. (2014). Improving power posterior estimation of statistical evidence. *Statistics and Computing*, *24*(5), 709–723. <https://doi.org/10.1007/s11222-013-9397-1>
- Friel, N., & Pettitt, A. N. (2008a). Marginal likelihood estimation via power posteriors. *Journal of the Royal Statistical Society: Series B (Statistical Methodology)*, *70*(3), 589–607. <https://doi.org/10.1111/j.1467-9868.2007.00650.x>
- Friel, N., & Pettitt, A. N. (2008b). Marginal likelihood estimation via power posteriors. *Journal of the Royal Statistical Society. Series B*, *70*(3), 589–607. <https://doi.org/10.1111/j.1467-9868.2007.00650.x>
- Gelman, A., & Meng, X.-L. (1998). Simulating normalizing constants: From importance sampling to bridge sampling to path sampling. *Statistical Science*, *13*, 163–185. <https://doi.org/10.1214/ss/1028905934>
- Gelman, A., Roberts, G. O., & Gilks, W. R. (1996). Efficient metropolis jumping rules. *Bayesian statistics*, *5*, 599–608.
- Gelman, A., & Rubin, D. B. (1992). Inference from iterative simulation using multiple sequences. *Statistical Science*, *7*(4), 457–472. <https://doi.org/10.1214/ss/1177011136>
- Geweke, J. (1992). Evaluating the accuracy of sampling-based approaches to the calculations of posterior moments. *Bayesian statistics*, *4*, 641–649.
- Gómez-Hernández, J. J., & Wen, X.-H. (1998). To be or not to be multi-Gaussian? A reflection on stochastic hydrogeology. *Advances in Water Resources*, *21*(1), 47–61. [https://doi.org/10.1016/S0309-1708\(96\)00031-0](https://doi.org/10.1016/S0309-1708(96)00031-0)
- Green, P. J. (1995). Reversible jump Markov chain Monte Carlo computation and Bayesian model determination. *Biometrika*, *82*(4), 711–732. <https://doi.org/10.1093/biomet/82.4.711>
- Grzegorzczak, M., Aderhold, A., & Husmeier, D. (2017). Targeting Bayes factors with direct-path non-equilibrium thermodynamic integration. *Computational Statistics*, *32*(2), 717–761. <https://doi.org/10.1007/s00180-017-0721-7>
- Guardiano, F. B., & Srivastava, R. M. (1993). Multivariate geostatistics: Beyond bivariate moments. In A. Soares (Ed.), *Geostatistics Tróia '92* (pp. 133–144). Dordrecht: Springer. [https://doi.org/10.1007/978-94-011-1739-5\\_12](https://doi.org/10.1007/978-94-011-1739-5_12)
- Gull, S. F. (1988). Bayesian inductive inference and maximum entropy. In G. J. Erickson, & C. R. Smith (Eds.), *Maximum-entropy and Bayesian methods in science and engineering* (Vol. 31–32, pp. 53–74). Cambridge: Springer. [https://doi.org/10.1007/978-94-009-3049-0\\_4](https://doi.org/10.1007/978-94-009-3049-0_4)
- Hammersley, J. M., & Handscomb, D. C. (1964). *Monte Carlo methods* (Vol. 1, VIII, pp. 178). Netherlands: Springer. <https://doi.org/10.1007/978-94-009-5819-7>
- Hansen, T. M., Cordua, K. S., & Mosegaard, K. (2012). Inverse problems with non-trivial priors: Efficient solution through sequential Gibbs sampling. *Computational Geosciences*, *16*(3), 593–611. <https://doi.org/10.1007/s10596-011-9271-1>
- Harbaugh, A. W. (2005). MODFLOW-2005 The US Geological Survey modular ground-water model: The ground-water flow process. US Department of the Interior, US Geological Survey Reston.
- Harvey, C., & Gorelick, S. M. (2000). Rate-limited mass transfer or macrodispersion: Which dominates plume evolution at the Macrodispersion Experiment (MADE) site? *Water Resources Research*, *36*(3), 637–650. <https://doi.org/10.1029/1999WR900247>
- Höhna, S., Landis, M. L., & Huelsenbeck, J. P. (2017). Parallel power posterior analyses for fast computation of marginal likelihoods in phylogenetics. <https://doi.org/10.1101/104422>

- Hu, L., & Chugunova, T. (2008). Multiple-point geostatistics for modeling subsurface heterogeneity: A comprehensive review. *Water Resources Research*, *44*, W11413. <https://doi.org/10.1029/2008WR006993>
- Jäggi, C., Straubhaar, J., & Renard, P. (2017). Posterior population expansion for solving inverse problems. *Water Resources Research*, *53*, 2902–2916. <https://doi.org/10.1002/2016WR019550>
- Jefferys, W. H., & Berger, J. (1992). Ockham's razor and Bayesian analysis. *American Scientist*, *80*(1), 64–72.
- Jeffreys, H. (1935). Some tests of significance, treated by the theory of probability. *Mathematical Proceedings of the Cambridge Philosophical Society*, *31*(2), 203–222. <https://doi.org/10.1017/S030500410001330X>
- Jeffreys, H. (1939). *Theory of probability* (3rd ed.). Oxford: Oxford University Press.
- Journel, A., & Zhang, T. (2006). The necessity of a multiple-point prior model. *Mathematical Geology*, *38*(5), 591–610. <https://doi.org/10.1007/s11004-006-9031-2>
- Kass, R. E., Carlin, B. P., Gelman, A., & Neal, R. M. (1998). Markov chain Monte Carlo in practice: A roundtable discussion. *The American Statistician*, *52*(2), 93–100. <https://doi.org/10.1080/00031305.1998.10480547>
- Kass, R. E., & Raftery, A. E. (1995). Bayes factors. *Journal of the American Statistical Association*, *90*(430), 773–795. <https://doi.org/10.1080/01621459.1995.10476572>
- Kerrou, J., Renard, P., Franssen, H.-J. H., & Lunati, I. (2008). Issues in characterizing heterogeneity and connectivity in non-multigaussian media. *Advances in Water Resources*, *31*(1), 147–159. <https://doi.org/10.1016/j.advwatres.2007.07.002>
- Koltermann, C. E., & Gorelick, S. M. (1996). Heterogeneity in sedimentary deposits: A review of structure-imitating, process-imitating, and descriptive approaches. *Water Resources Research*, *32*(9), 2617–2658. <https://doi.org/10.1029/96WR00025>
- Künze, R., & Lunati, I. (2012). An adaptive multiscale method for density-driven instabilities. *Journal of Computational Physics*, *231*(17), 5557–5570. <https://doi.org/10.1016/j.jcp.2012.02.025>
- Laloy, E., Héroult, R., Jacques, D., & Linde, N. (2018). Training-image based geostatistical inversion using a spatial generative adversarial neural network. *Water Resources Research*, *54*, 381–406. <https://doi.org/10.1002/2017WR022148>
- Laloy, E., Linde, N., Jacques, D., & Mariethoz, G. (2016). Merging parallel tempering with sequential geostatistical resampling for improved posterior exploration of high-dimensional subsurface categorical fields. *Advances in Water Resources*, *90*, 57–69. <https://doi.org/10.1016/j.advwatres.2016.02.008>
- Laloy, E., & Vrugt, J. A. (2012). High-dimensional posterior exploration of hydrologic models using multiple-try DREAM<sub>ZS</sub> and high-performance computing. *Water Resources Research*, *48*, W01526. <https://doi.org/10.1029/2011WR010608>
- Lark, R., Thorpe, S., Kessler, H., & Mathers, S. (2014). Interpretative modelling of a geological cross section from boreholes: Sources of uncertainty and their quantification. *Solid Earth*, *5*(2), 1189–1203. <https://doi.org/10.5194/se-5-1189-2014>
- Lartillot, N., & Philippe, H. (2006). Computing Bayes factors using thermodynamic integration. *Systematic Biology*, *55*(2), 195–207. <https://doi.org/10.1080/10635150500433722>
- Lewis, S. M., & Raftery, A. E. (1997). Estimating Bayes factors via posterior simulation with the Laplace-Metropolis estimator. *Journal of the American Statistical Association*, *92*(438), 648–655. <https://doi.org/10.1080/01621459.1997.10474016>
- Li, X., Mariethoz, G., Lu, D., & Linde, N. (2016). Patch-based iterative conditional geostatistical simulation using graph cuts. *Water Resources Research*, *52*, 6297–6320. <https://doi.org/10.1002/2015WR018378>
- Linde, N. (2014). Falsification and corroboration of conceptual hydrological models using geophysical data. *Wiley Interdisciplinary Reviews: Water*, *1*(2), 151–171. <https://doi.org/10.1002/wat2.1011>
- Linde, N., Ginsbourger, D., Irving, J., Nobile, F., & Doucet, A. (2017). On uncertainty quantification in hydrogeology and hydrogeophysics. *Advances in Water Resources*, *110*, 166–181. <https://doi.org/10.1016/j.advwatres.2017.10.014>
- Linde, N., Lochbühler, T., Dogan, M., & Van Dam, R. L. (2015). Tomogram-based comparison of geostatistical models: Application to the Macrodispersion Experiment (MADE) site. *Journal of Hydrology*, *531*, 543–556. <https://doi.org/10.1016/j.jhydrol.2015.10.073>
- Linde, N., Renard, P., Mukerji, T., & Caers, J. (2015a). Geological realism in hydrogeological and geophysical inverse modeling: A review. *Advances of Water Resources*, *86*, 86–101. <https://doi.org/10.1016/j.advwatres.2015.09.019>
- Liu, P., Elshall, A. S., Ye, M., Beerli, P., Zeng, X., Lu, D., & Tao, Y. (2016). Evaluating marginal likelihood with thermodynamic integration method and comparison with several other numerical methods. *Water Resources Research*, *52*, 734–758. <https://doi.org/10.1002/2014WR016718>
- Liu, G., Zheng, C., Tick, G. R., Butler, J. J., & Gorelick, S. M. (2010). Relative importance of dispersion and rate-limited mass transfer in highly heterogeneous porous media: Analysis of a new tracer test at the Macrodispersion Experiment (MADE) site. *Water Resources Research*, *46*, W03524. <https://doi.org/10.1029/2009WR008430>
- Lochbühler, T., Pirot, G., Straubhaar, J., & Linde, N. (2014). Conditioning of multiple-point statistics facies simulations to tomographic images. *Mathematical Geosciences*, *46*(5), 625–645. <https://doi.org/10.1007/s11004-013-9484-z>
- Lochbühler, T., Vrugt, J. A., Sadegh, M., & Linde, N. (2015). Summary statistics from training images as prior information in probabilistic inversion. *Geophysical Journal International*, *201*(1), 157–171. <https://doi.org/10.1093/gji/ggv008>
- MacKay, D. J. (1992). Bayesian interpolation. *Neural Computation*, *4*(3), 415–447. <https://doi.org/10.1162/neco.1992.4.3.415>
- Maliva, R. G. (2016). *Aquifer characterization techniques*. Berlin: Springer. <https://doi.org/10.1007/978-3-319-32137-0>
- Mariethoz, G., & Caers, J. (2014). *Multiple-point geostatistics: Stochastic modeling with training images*. Chichester, UK: John Wiley & Sons. <https://doi.org/10.1002/9781118662953>
- Mariethoz, G., Renard, P., & Caers, J. (2010a). Bayesian inverse problem and optimization with iterative spatial resampling. *Water Resources Research*, *46*, W11530. <https://doi.org/10.1029/2010WR009274>
- Mariethoz, G., Renard, P., & Straubhaar, J. (2010). The direct sampling method to perform multiple-point geostatistical simulations. *Water Resources Research*, *46*, W11536. <https://doi.org/10.1029/2008WR007621>
- Mosegaard, K., & Tarantola, A. (1995). Monte Carlo sampling of solutions to inverse problems. *Journal of Geophysical Research*, *100*(B7), 12,431–12,447. <https://doi.org/10.1029/94JB03097>
- Oates, C. J., Papamarkou, T., & Girolami, M. (2016). The controlled thermodynamic integral for Bayesian model evidence evaluation. *Journal of the American Statistical Association*, *111*(514), 634–645. <https://doi.org/10.1080/01621459.2015.1021006>
- Pirot, G., Cardiff, M., Mariethoz, G., Bradford, J., & Linde, N. (2017b). Towards 3D probabilistic inversion with graphcuts. 23rd European Meeting of Environmental and Engineering Geophysics.
- Pirot, G., Linde, N., Mariethoz, G., & Bradford, J. H. (2017). Probabilistic inversion with graph cuts: Application to the Boise Hydrogeophysical Research Site. *Water Resources Research*, *53*, 1231–1250. <https://doi.org/10.1002/2016WR019347>
- Pirot, G., Renard, P., Huber, E., Straubhaar, J., & Huggenberger, P. (2015). Influence of conceptual model uncertainty on contaminant transport forecasting in braided river aquifers. *Journal of Hydrology*, *531*, 124–141. <https://doi.org/10.1016/j.jhydrol.2015.07.036>
- Randle, C. H., Bond, C. E., Lark, R. M., & Monaghan, A. A. (2018). Can uncertainty in geological cross-section interpretations be quantified and predicted? *Geosphere*, *14*, 1087–1100. <https://doi.org/10.1130/GES01510.1>

- Refsgaard, J. C., Christensen, S., Sonnenborg, T. O., Seifert, D., Højberg, A. L., & Troldborg, L. (2012). Review of strategies for handling geological uncertainty in groundwater flow and transport modeling. *Advances in Water Resources*, *36*, 36–50. <https://doi.org/10.1016/j.advwatres.2011.04.006>
- Refsgaard, J. C., & Henriksen, H. J. (2004). Modelling guidelines—Terminology and guiding principles. *Advances in Water Resources*, *27*(1), 71–82. <https://doi.org/10.1016/j.advwatres.2003.08.006>
- Rehfeldt, K. R., Boggs, J. M., & Gelhar, L. W. (1992). Field study of dispersion in a heterogeneous aquifer: 3. Geostatistical analysis of hydraulic conductivity. *Water Resources Research*, *28*(12), 3309–3324. <https://doi.org/10.1029/92WR01758>
- Remy, N., Boucher, A., & Wu, J. (2009). *Applied geostatistics with SGeMS: A user's guide*. Cambridge: Cambridge University Press.
- Renard, P., & Allard, D. (2013). Connectivity metrics for subsurface flow and transport. *Advances in Water Resources*, *51*, 168–196. <https://doi.org/10.1016/j.advwatres.2011.12.001>
- Renard, P., Demougeot-Renard, H., & Froidevaux, R. (2005). *Geostatistics for environmental applications*. Berlin: Springer. <https://doi.org/10.1007/s11004-018-9733-2>
- Rojas, R., Feyen, L., & Dassargues, A. (2008). Conceptual model uncertainty in groundwater modeling: Combining generalized likelihood uncertainty estimation and Bayesian model averaging. *Water Resources Research*, *44*, W12418. <https://doi.org/10.1029/2008WR006908>
- Ronayne, M. J., Gorelick, S. M., & Zheng, C. (2010). Geological modeling of submeter scale heterogeneity and its influence on tracer transport in a fluvial aquifer. *Water Resources Research*, *46*, W10519. <https://doi.org/10.1029/2010WR009348>
- Scheidt, C., Li, L., & Caers, J. (2018). *Quantifying uncertainty in subsurface systems* (Vol. 236). New York: John Wiley & Sons. <https://doi.org/10.1002/9781119325888>
- Schöniger, A., Wöhling, T., Samaniego, L., & Nowak, W. (2014). Model selection on solid ground: Rigorous comparison of nine ways to evaluate Bayesian model evidence. *Water Resources Research*, *50*, 9484–9513. <https://doi.org/10.1002/2014WR016062>
- Skilling, J. (2004). Nested sampling. *AIP Conference Proceedings*, *735*, 395–405. <https://doi.org/10.1063/1.1835238>
- Skilling, J. (2006). Nested sampling for general Bayesian computation. *Bayesian analysis*, *1*(4), 833–859. <https://doi.org/10.1214/06-BA127>
- Strebelle, S. (2002). Conditional simulation of complex geological structures using multiple-point statistics. *Mathematical Geology*, *34*(1), 1–21. <https://doi.org/10.1023/A:1014009426274>
- Vlugt, T. J., & Smit, B. (2001). On the efficient sampling of pathways in the transition path ensemble. *PhysChemComm*, *4*(2), 11–17. <https://doi.org/10.1039/B009865P>
- Volpi, E., Schoups, G., Firmani, G., & Vrugt, J. (2017). *Sworn testimony of the model evidence: Gaussian Mixture Importance (GAME) sampling* (Vol. 53, pp. 6133–6158). <https://doi.org/10.1002/2016WR020167>
- Xie, W., Lewis, P. O., Fan, Y., Kuo, L., & Chen, M.-H. (2011). Improving marginal likelihood estimation for Bayesian phylogenetic model selection. *Systematic Biology*, *60*(2), 150–160. <https://doi.org/10.1093/sysbio/syq085>
- Zahner, T., Lochbühler, T., Mariethoz, G., & Linde, N. (2016). Image synthesis with graph cuts: A fast model proposal mechanism in probabilistic inversion. *Geophysical Journal International*, *204*(2), 1179–1190. <https://doi.org/10.1093/gji/ggv517>
- Zeng, X., Ye, M., Wu, J., Wang, D., & Zhu, X. (2018). Improved nested sampling and surrogate-enabled comparison with other marginal likelihood estimators. *Water Resources Research*, *54*, 797–826. <https://doi.org/10.1002/2017WR020782>
- Zheng, C. (2010). MT3DMS v5. 3 supplemental user's guide. Department of Geological Sciences University of Alabama, Tuscaloosa, Alabama.
- Zheng, C., Bianchi, M., & Gorelick, S. M. (2011). Lessons learned from 25 years of research at the MADE site. *Groundwater*, *49*(5), 649–662. <https://doi.org/10.1111/j.1745-6584.2010.00753.x>
- Zheng, C., & Gorelick, S. M. (2003). Analysis of solute transport in flow fields influenced by preferential flowpaths at the decimeter scale. *Groundwater*, *41*(2), 142–155. <https://doi.org/10.1111/j.1745-6584.2003.tb02578.x>
- Zinn, B., & Harvey, C. F. (2003). When good statistical models of aquifer heterogeneity go bad: A comparison of flow, dispersion, and mass transfer in connected and multivariate Gaussian hydraulic conductivity fields. *Water Resources Research*, *39*(3), 1051. <https://doi.org/10.1029/2001WR001146>